Active drag reduction of a high-drag Ahmed body based on steady blowing

B. F. Zhang[1, 2], K. Liu[1, 3], Y. Zhou[1, 4#], S. To[2] and J. Y. Tu[5]

[1]Institute for Turbulence-Noise-Vibration Interactions and Control, Shenzhen Graduate School, Harbin Institute of Technology, Shenzhen, China

[2]State Key Laboratory of Ultra-precision Machining Technology, Department of Industrial and System Engineering, The Hong Kong Polytechnic University, Hong Kong

[3]Department of Mechanical Engineering, The Hong Kong Polytechnic University, Hong Kong

[4]Digital Engineering Laboratory of Offshore Equipment, Shenzhen, China

[5]School of Engineering, RMIT University, Australia

[#]Corresponding author: yuzhou@hit.edu.cn

Abstract

Active drag reduction of an Ahmed body with a slant angle of 25°, corresponding to the high-drag regime, has been experimentally investigated at Reynolds number $Re = 1.7 \times 10^5$, based on the square root of the model cross-sectional area. Four individual actuations, produced by steady blowing, are applied separately around the edges of the rear window and vertical base, producing a drag reduction up to 6% ~ 14%. However, the combination of the individual actuations results in a drag reduction by 29%, higher than any previous drag reductions achieved experimentally and very close to the target (30%) set by automotive industries. Extensive flow measurements are performed, with and without control, using force balance, pressure scanner, hotwire, flow visualization and particle image velocimetry techniques. A marked change in the flow structure is captured in the wake of the body under control, including the flow separation bubbles, be over the rear window or behind the vertical base, and the C-pillar vortices. The change is linked to the pressure rise on the slant surface and the base. The mechanisms behind the effective control are proposed. The control efficiency is also estimated.

1. Introduction

There has been recently a renewed interest in finding new technologies to reduce aerodynamic drag and hence fuel consumption in automotive industry because of the issues of global warming and environmental pollution as well as high fuel costs. Many classes of transport and multifarious important applications stand to reap great rewards from the successful development of drag reduction (DR) technologies. Over 60% of the total fuel consumption of a typical car or truck running on a highway is due to aerodynamic drag (Metka & Gregory 2015). Every 10 percent reduction in aerodynamic drag on a vehicle means a fuel consumption saving of about 5% (e.g. Bellman *et al.* 2010). The reduced fuel consumption also implies less emission discharged by vehicles, which is now one of the major contributors to air pollution.

For the purpose of reducing vehicle drag, passive means such as flaps (e.g. Beaudoin & Aider 2008), vortex generators (e.g. Pujals *et al.* 2010), streamlining body shape and local body-shape modifications (e.g. Verzicco *et al*. 2002; Lucas *et al*. 2017) have achieved a great success. Nevertheless, the passive techniques are characterized by permanent fixtures. Once mounted, flaps or vortex generators are difficult to be removed or re-arranged. Furthermore, the passive techniques such as shaping vehicle bodies have made a great success, approaching the optimum. For example, the theoretical limit of the drag coefficient CD of vehicles is about 0.1 (Cengel & Cimbala 2010). A race car may reach 0.2 in CD, while Toyota Prius has achieved 0.26. On the other hand, active control has potential to reduce drag significantly further and achieves flexible flow modifications.

Rouméas *et al.*'s (2009a) numerical investigation demonstrated that steady blowing could reduce the drag of a square-back vehicle by 29%. European motor industry has set a target to reduce actively the aerodynamic drag of vehicles by at least 30% without restrictions on the comfort, storage or security of passengers (Bruneau *et al.* 2011). Naturally, active control has been given more and more attentions in the past decade or so, with a variety of actuations investigated, including steady blowing (e.g. Aubrun *et al.* 2011), steady but spanwise alternately arranged suction and blowing (e.g. Kim *et al.* 2004), suction and oscillatory blowing (e.g. Seifert *et al.* 2008), pulsed blowing and Coanda effect (e.g. Barros *et al.* 2014 and 2016), synthetic jet (e.g. Evstafyeva *et al*. 2017), and Plasma (Boucinha *et al.* 2011). See Choi *et al.* (2014) and Sudin *et al.* (2014) for recent reviews.

The generic Ahmed body (Ahmed *et al*. 1984) is perhaps the most widely studied simplified car model. This body has a curved forepart to prevent flow separation there, a straight middle body with a rectangular cross section and a rear part with a slanted surface, and may simulate different vehicle types depending on the slant angle φ which is measured clockwise from the streamwise direction to the slanted surface. The wake of this body consists of three major components: a separation bubble over the rear window, one pair of counter-rotating longitudinal C-pillar vortices, and two recirculation bubbles behind the vertical base. The interactions between the three types of coherent structures depend on φ and have a great effect on the aerodynamic drag of the body (e.g. Ahmed *et al*. 1984). Naturally, the aerodynamic drag coefficient also depends on φ. At relatively small φ, the C-pillar vortices occur. The two C-pillar vortices contribute to the drag and meanwhile induce a downwash between them, which enhances flow reattachment on the rear window. The combined effect is a DR. The drag reaches its minimum as φ increases to 12.5°. Above $\varphi = 15°$, the strength of the C-pillar vortices rises with increasing φ; so does the drag, with its maximum occurring at $\varphi = 30°$. A further increase in φ leads to the burst of the vortices and a sharp fall in the drag despite a fully separated flow. As such, the wake of the Ahmed body may be divided into two distinct regimes, i.e. the high-drag regime at $\varphi \leq 30°$ and the low-drag regime at $\varphi > 30°$ (Hucho & Sovran 1993).

Controlling the interactions between the three types of coherent structures is the key of DR techniques. Manipulating the rear window and the vertical base will directly influence the three types of coherent structures (Gad-el-Hak 2000). Therefore, it is feasible to implement wall-based control schemes for DR. Active flow control techniques based on steady blowing of air through slots or arrays of orifices have been widely applied numerically or experimentally for the DR of an Ahmed body of $\varphi = 25°$, corresponding to the high-drag flow regime (Brunn *et al*. 2007; Wassen *et al*. 2008, 2009, 2010; Aubrun *et al*. 2011; Bruneau *et al*. 2011). In their LES simulation, Wassen & Thiele (2010) deployed vertically upward steady blowing along the upper and two side edges of the rear window and 45° inward along the lower and two side edges of the base of an Ahmed model ($\varphi = 25°$), emulating Beaudoin & Aider's (2008) flap-based passive control ($\varphi = 30°$). As they examined blowing at a fixed exit velocity and a single bowing angle, without optimizing control parameters, a rather limited DR, 10.2%, was obtained. In contrast, Beaudoin & Aider (2008) deployed passive flaps fixed on every edge around the rear window and the vertical base of the model and obtained the optimal angle, for each flap, thus achieving a DR of 25%. Aubrun *et al*. (2011) mounted an array of steady microjets, blowing normal to the wall, on the rear window of an Ahmed body ($\varphi = 25°$), achieving experimentally a DR up to 14%, quite comparable to Rouméas *et al*.'s (2009b) DR, attained numerically using steady suction through a slot, for a fastback vehicle model whose roof slants continuous down at the back. In their DNS investigation ($Re = 9.6 \times 10^3$), Bruneau *et al.* (2011) deployed a transverse suction slot on the top of the rear window of the Ahmed model ($\varphi = 25°$) and a transverse blowing slot at mid of the vertical base, resulting in reattached flow over the rear window and breakdown of the large recirculation behind the base and achieving a DR of 7%. They then used steady blowing on both sides of the rear window to impair the C-pillar vortices, producing a DR of 11%. When both actuations were applied simultaneously, a 13% DR was achieved. These efforts, albeit with a limited success, are encouraging.

Unsteady excitation may capitalize the natural instability of turbulence and greatly improve the control efficiency. For example, given the same control performance, Yang & Zhou (2016) saved three quarters of input energy in the manipulation of a turbulent jet when using unsteady minijets to replace steady minijets. Naturally, unsteady excitation has been explored. Various actuators have been used, including synthetic jets (Glezer & Amitay 2002), dielectric barrier discharge plasma (Corke *et al*. 2010) and fluidic actuators (e.g. Cattafesta & Sheplak 2011). In their experimental study on the active DR of an Ahmed body with $\varphi = 25°$, Joseph *et al.* (2012) deployed an array of pulsed jets, generated through spanwise-aligned rectangular orifices and placed upstream of the upper edge of the rear window, blowing normal to the roof. The jets induced pairs of streamwise counter-rotating vortices, causing a change in the boundary layer and postponing flow separation at the upper edge of the slanted surface. Yet, the reduced separation bubble led to a more pronounced pressure loss within the core of the C-pillar vortices. As a result, a maximum DR of about 8% was produced. The result was reconfirmed by Kourta & Leclerc (2013), who deployed an array of synthetic jets at the upper edge of the rear window. Park *et al.* (2013) applied synthetic jet array actuation along the upper edge of the rear window to control the wake of two different Ahmed model configurations with $\varphi = 25°$ and 35°, producing a DR of 3% and a drag increase, respectively. Boucinha *et al*. (2011) used dielectric barrier discharge plasma actuator placed near the upper edge of the rear window ($\varphi = 25°$), suppressing flow separation and reducing drag by 8%. In their experimental study on the active DR of an Ahmed body ($\varphi = 35°$), Gilliéron & Kourta (2013) deployed an array of pulsed jets, issued through rectangular slots near the rounded upper edge of the rear window. Both the upper and lower recirculation regions were enlarged longitudinally and their vortex centers moved downstream, resulting in a velocity decrease near the surfaces of the rear window and the base. The strength of the two C-pillar vortices was also weakened. They achieved an impressive DR of 20%. Barros *et al.* (2016) deployed pulsed jets around the four edges of the vertical base of a square-back Ahmed body ($\varphi = 0°$), resulting in a maximum DR by about 11% ($Re = 3.5 \times 10^5$). With the edges rounded, i.e. a combination of passive and active methods, the ensuing Coanda effect raised the maximum DR to 18%.

Past investigations on active DR have greatly enriched our knowledge in the control of the Ahmed model wake but also raised a number of issues. Firstly, these efforts have mostly achieved a rather limited success, as summarized in table 1; the maximum DR obtained experimentally is only about 14% for the high-drag model (Aubrun *et al.* 2011), considerably below the target (30%) set by automotive industries (Bruneau *et al.* 2011) and even below what is achieved via passive flaps (Beaudoin & Aider 2008). Secondly, most of the previous studies focused on controlling one of the three types of coherent structures in the wake, neglecting the other two and their interactions. In their experimental and numerical investigations on the active DR of an Ahmed model, Brunn *et al.* (2007) found that, at $\varphi = 35°$, the synthetic jet placed at mid of the upper edge of the rear window reduced the flow separation region but meanwhile triggered the development of C-pillar vortices; at $\varphi = 25°$, constant blowing near the two upper corners of the rear window weakened C-pillar vortices but increased the flow separation region. As a result, no significant DR was achieved. It is therefore plausible that an effective and efficient active DR technique requires a combination of different actuations schemes, i.e. producing actuations at different locations and orientations, which could not only weaken C-pillar vortices but also increase the pressure on the rear window and the vertical base. So far, there have been only a few studies reported on the control of an Ahmed model, which have deployed a combination of different actuations. The optimum combination of different actuations to reduce effectively and efficiently drag remains elusive. Thirdly, the ratio of the saved power because of DR to the control input power, which is a crucial indicator to evaluate the efficiency of active DR (Choi *et al.* 2008), has been seldom studied previously for the Ahmed model of $\varphi = 25°$. Finally, numerous numerical studies on the active DR of the Ahmed body call for a more complete experimental data base for the validation of the CFD codes.

This work aims to address the above-mentioned issues, through a rather extensive experimental investigation on the active DR of the Ahmed model of $\varphi = 25°$, on the basis of our recent improved understanding of flow physics. Zhang *et al.* (2015) conducted a relatively thorough investigation on the flow structure around a high-drag Ahmed body ($\varphi = 25°$). A conceptual model of the flow structure (figure 1) was proposed. Unlike the model proposed by Ahmed *et al.* (1984), this model embraces both steady and unsteady coherent structures around the body and even the *St* range of unsteady coherent structures. Experimental details are given in §2. The results are presented in §3, including the uncontrolled flow, the effects of individual and combined actuations on the drag, associated physics/mechanisms and the control efficiency. This work is concluded in §4.

2. Experimental details

2.1. *Experimental set-up*

Experiments were carried out in a closed circuit wind tunnel with a 5.6-m-long, 1.0-m-high and 0.8-m-wide rectangular test section. The flow non-uniformity is less than 0.1% and the longitudinal turbulence intensity is within 0.4% in the test section. Figure 2(*a*) shows schematically the experimental setup. A flat plate of 2.6 m × 0.78 m × 0.015 m with a clipper-built leading edge is installed horizontally, 0.1 m above the floor of the test section, as a raised floor to control the boundary layer thickness. Its leading edge is 2 m downstream of the exit plane of the tunnel contraction.

The vehicle model was a ½-scaled Ahmed body with $\varphi = 25°$, 0.522 m in length (L), 0.1945 m in width (B) and 0.144 m in height (H), supported by four cylindrical struts of 15 mm in diameter (figure 2*b*,*c*). Its front end was 0.3 m, where the boundary layer thickness was about 4 mm at a free-stream velocity of 12 m/s, downstream of the floor leading edge. The clearance between the model underside and the surface of the raised floor was 25 mm. The blockage ratio of the frontal surface of the model to the rectangular test section above the raised floor was around 3.9%. The right-handed Cartesian coordinate system (x, y, z) is defined such that its origin o is at the midpoint of the lower edge of the model vertical base (figure 2*c*). In this paper, superscript asterisk denotes normalization by the square root of model frontal area $\sqrt{A}$ (= 0.167 m) and/or the free-stream velocity U_∞; for example, $f^*=f\sqrt{A}/U_\infty$, $\omega_x^* = \omega_x\sqrt{A}/U_\infty$ and $\omega_y^* = \omega_y\sqrt{A}/U_\infty$, where f is frequency, ω_x and ω_y are the instantaneous vorticity components in the x and y directions, respectively. The instantaneous velocity components in the x, y and z directions are designated as U, V and W, which can be decomposed as $U = \overline{U} + u$, $V = \overline{V} + v$ and $W = \overline{W} + w$, respectively, where overbar denotes time-averaging, and u, v and w are the fluctuating velocity components.

Four different actuations, all steady blowing, were deployed over the rear window and behind the vertical base of the model, referred to as S_1, S_2, S_3 and S_4 (figure 3*a*). S_1 was produced by an array of microjets issued from 47 circular orifices of 1 mm in diameter, equally separated by 2 mm, along a line 3 mm parallel to and downstream of the upper edge of the rear window. S_2 was generated through two slots of 0.8 mm in width and 96 mm in length, arranged separately along the two side edges of the rear window. The distance between the slot and the side edge of the slanted surface was 1 mm. S_3 and S_4 were generated by two arrays of microjets, each consisting of 39 circular orifices of 1 mm in diameter, equally separated by 2 mm, along the upper and lower edges of the vertical base, respectively. The blowing angles θ_{S1}, θ_{S2}, θ_{S3} and θ_{S4} of S_1, S_2, S_3 and S_4 (figure 3*a*), respectively, may be varied. The S_1 was tested for DR at θ_{S1} = 0°, 30°, 65° and 90°, and S_2 was investigated at θ_{S2} = 30°, 60° and 90°. The angles θ_{S1} = 65° and θ_{S2} = 90° correspond to the blowing direction normal to the slanted surface. Five different blowing angles, i.e. -45°, -30°, 0°, 30° and 45°, were examined for each of S_3 and S_4.

S_1, S_2, S_3 and S_4 were issued from five separate chambers, which were imbedded in the model. The exit width of each chamber is $2l_s^*$ (figure 3*b*). A flexible tube, passing through the hollow strut of the model, connected each chamber with air supply. The tube was hung vertically downwards from the model before reaching the ground, resulting in a negligibly small horizontal force between the tube and the ground. The pressure of air supply was adjusted using a high precision pressure regulator (SMC IR3020). The flow rate through the chamber was measured by a flow meter with a measuring range of 0 ~ 200 l/min with an accuracy of ±1 l/min. Following McNally *et al.* (2015) and Kumar & Alvi (2006), the blowing ratio BR^{Si} and the momentum coefficient C_μ^{Si} of S_i (i = 1, 2, 3, 4) are defined by

$$BR^{\mathrm{Si}}=\frac{V_{\mathrm{Si}}}{U_\infty}, \tag{2.1}$$

and

$$C_\mu^{\mathrm{Si}}=\frac{N_{\mathrm{Si}}\,\rho_{\mathrm{air}}\,Q_{\mathrm{Si}}\,V_{\mathrm{Si}}}{0.5\,\rho_{\mathrm{air}}\,U_\infty^2\,A}, \tag{2.2}$$

where N_{Si} is the number of microjets or slot jets, ρ_{air} is the air density, and Q_{Si} and V_{Si} are the volume flow rate and the exit velocity of a microjet or slot jet, respectively.

Figure 4 presents the time-averaged centerline velocity $\overline{V}_s$ measured using a Pitot static tube connected to an electronic manometer at 1 mm above the jet exit for different exit transverse positions l_s^* of the four actuations. The variations in $\overline{V}_s$ is less than 10% for each actuation, as compared with the mean velocity along the transverse direction, which is indicated by the dashed line. The variation in $\overline{V}_s$ results from the diverging surface upstream of the exit (figure 3*b*), similarly to that produced by Bideaux *et al.* (2011) whose actuation jets were issued from a diffusor.

2.2. *Flow measurements*

A single hotwire was placed along the y-direction at $x^* = 0.4$, $y^* = 0$ and $z^* = 0.18$ to measure the velocity fluctuations u_{xz} in the (x, z) plane to detect the predominant frequencies in the wake. The sensing element was a tungsten wire of 5 μm in diameter and about 1 mm in length. The wire was operated on a constant temperature circuit (Dantec Streamline) at an overheat ratio of 1.8. The signal from the wire was offset, amplified and low-pass filtered at a cut-off frequency of 1.0 kHz, and digitized at a sampling frequency f_s of 3.0 kHz using a 16-bit A/D converter (NI PCI-6143). The sampling duration was 180 sec, producing a total of 5.4×10^5 data for each record. At least three records were obtained for each measurement location. The fast Fourier transform (FFT) algorithm was used to calculate the power spectral density function, E_u, of u_{xz}, which is normalized by the variance of u_{xz} so that its integration over the entire frequency range is unity. The FFT window size N_w was 4096. The frequency resolution Δf in the spectral analysis depends on f_s and N_w, viz. $\Delta f = f_s/N_w$ (e.g. Zhou *et al.* 2012) = 0.73 Hz.

A Dantec high-speed two-dimensional (2D) particle image velocimetry (PIV) system was used to measure the wake of the Ahmed model. The flow was seeded with smoke generated from paraffin oil, with the particles of about 1 μm in diameter. The response time (τ_p) of the particles is calculated by

$$\tau_p=\frac{(\gamma-1)D_p^2}{18\nu}, \tag{2.3}$$

where γ is the ratio of the density of the particle to ρ_{air}, D_p is the particle diameter and ν is the kinematic viscosity of the air (e.g. Nabavi *et al.* 2008). The τ_p is about 3 μs from equation (2.3). Following Gomes-Fernandes *et al.* (2012), the particle Stokes number St_p is given by

$$St_p = \tau_p / \tau_\eta, \tag{2.4}$$

where τ_η is the Kolmogorov time scale. The St_p must be less than 1 for the particles to follow reliably the motion of smallest eddies. Howard & Pourquie (2002) proposed an estimation of the Kolmogorov length scale η_v for the Ahmed body wake, viz.

$$\eta_v \approx 0.51Re^{-0.75}L. \tag{2.5}$$

The η_v is 0.03 mm, and τ_η is then 70 μs, resulting in $St_p \approx 0.04$, indicating that the particles can track well the velocity fluctuations of flow.

Flow illumination was provided by two New Wave standard pulsed laser sources of 532 nm in wavelength, each with a maximum energy output of 30 mJ/pulse. Each laser pulse lasted for 0.01 μs. One charge-coupled device (CCD) camera (PhantomV641, double frames, with a resolution of 2560 × 1600 pixels) was used to capture particle images. Synchronization between image taking and flow illumination was provided by the Dantec timer box 80N77. PIV measurements were performed in the (x, z) planes at $y^* = 0$ (symmetry plane) and at $y^* = 0.45$, and the (y, z) plane at $x^* = 0.2$. The PIV images covered an area of $x^* = -0.69 \sim 1.45$ and $z^* = -0.10 \sim 1.24$ in the (x, z) plane and $y^* = -0.99 \sim 0.99$ and $z^* = -0.10 \sim 1.14$ in the (y, z) plane. The image magnifications in both directions of each plane were identical, about 140 and 130 μm/pixel in the (x, z) and (y, z) planes, respectively. The intervals between two successive pulses were 60 μs and 20 μs for measurements in the (x, z) and (y, z) planes, respectively. In processing PIV images, the adaptive PIV method (Dynamic Studio software) was used with the minimum interrogation area size of 32 × 32 pixels and the maximum size of 64 × 64 pixels, and the grid step size of 16 × 16 pixels, producing 160 × 100 in-plane velocity vectors and the same number of vorticity data ω_x^* or ω_y^*. A total of 1800 images were captured for each case, with a trigger rate of 350 Hz in the double frame mode.

The model surface, raised floor and tunnel working section walls hit by the laser sheet were all painted black to minimize reflection. Nevertheless, the reflection of laser light from the rear window and the vertical base was still discernible in the PIV images. It has been confirmed that the region affected by this reflection in the (x, z) plane was within a distance of $\lambda \approx 1.5$ mm or $\lambda^* \approx 0.009$ from the slanted surface. In the absence of control, the length of the flow separation region, i.e. the longitudinal length where $\overline{U} \leq 0$, over the slanted surface is about $0.1\sqrt{A}$ in the symmetry plane. Thus, the reflection causes an uncertainty of 9% in the determination of this length. On the other hand, the region affected by this reflection is within a distance of $\lambda \approx 1$ mm or $\lambda^* \approx 0.006$ from the vertical base surface, about 1% of the upper and lower recirculation bubble lengths. The region affected by this reflection is within a distance of $\lambda \approx 2$ mm or $\lambda^* \approx 0.012$ from the floor surface in both (x, z) and (y, z) planes. All these affected regions are masked with black color to remove their influence during processing the PIV images.

The uncertainty of PIV measurements arises from a number of sources, including time delay between two successive frames, density of seeding particles, out-of-plane motion of particles, interrogation window size, etc.; it remains to be a challenge to determine exact contributions from individual sources (e.g. Raffel *et al.* 2007). One approach that has been widely adopted to determine the PIV measurement uncertainty is the image matching analysis (e.g. Quinn *et al.* 2014; Rajamanickam & Basu 2017). This method identifies particle image pairs in two successive exposures according to the measured displacement vectors, and evaluates the residual distance or particle disparity between the particle image pairs, which depends mainly on the velocity variation caused by a finite laser sheet thickness and dictates the uncertainty of velocity measurements. Further details of this technique can be found in Sciacchitano *et al.* (2013). In the (x, z) planes of y^* = 0 and 0.45, the present seeding densities are at least 10 particles per interrogation window. The root-mean-square (RMS) value of the disparity was found, based on the Dynamic Studio software, to be 0.07 pixel in both x and z directions, resulting in the uncertainties, σ_U and σ_W, in U and W of 1%U_∞, respectively. Following Wen *et al.* (2015), the uncertainty ($\sigma_{\omega y}$) of the spanwise vorticity ω_y is given by

$$\sigma_{\omega y} = \sigma_U / \Delta x, \tag{2.6}$$

where Δx is the grid size (16 pixels or 2.2 mm). The highest magnitudes of $\overline{\omega_y^*}$ were measured to be about 25 and 30 in the (x, z) planes of y^* = 0 and 0.45 (over the rear window), respectively, the corresponding $\sigma_{\omega y}$ being 3.1% and 2.6% of the maximum vorticities, respectively. In the (x, z) plane of y^* = 0.45, the mean out-of-plane velocity is 0.7 m/s estimated from the PIV-measured ($\overline{V}$, $\overline{W}$) and the out-of-plane displacement is 0.04 mm, around 4% of the laser light thickness (1 mm). In the plane of y^* = 0, the mean out-of-plane velocity is less than 0.1 m/s and the resultant displacement is within 0.6% of the laser thickness. In the (y, z) plane, the laser sheet was made thicker, approximately 2 mm, to capture an adequate number of seeding particles (Huang *et al.* 2006). At least 10 particles occur in each interrogation window. The RMS value of the disparity in this plane was found to be 0.09 pixel, slightly larger than that (0.07 pixel) in the (x, z) plane. This difference is ascribed to the increased out-of-plane motion of particles in the thickened laser sheet. The uncertainties, σ_V and σ_W, in V and W, are estimated to be 3% of U_∞. The uncertainty ($\sigma_{\omega x}$) of the streamwise vorticity is found to be about 14% of the maximum vorticity which is 13 at U_∞ = 15m/s. The out-of-plane displacement is 0.3 mm, approximately 15% of the laser sheet thickness.

The number of images, denoted by N, needs to be adequately large so that the time-averaged data are converged. In their experimental study on the wake of Ahmed bodies, Wang *et al.* (2013) estimated the convergence of the percentage difference (δ) of time-averaged quantities β_N with increasing N, defined as

$$\delta = \frac{\beta_N - \beta_{N\text{-}\Delta N}}{\beta_N} \times 100\%, \tag{2.7}$$

where β denotes $\overline{U}$, $\overline{W}$, and $\overline{\omega_y^*}$, and subscript 'N' or '$N - \Delta N$' is the number of images (ΔN is the increment in N). The calculated δ at different positions in the symmetry plane of the wake is converged to less than ±1% at $N \approx 800$ for all the time-averaged quantities. Then, 1800 flow images presently captured should be adequate for determining the mean flow fields.

Flow visualization was conducted using the same PIV system. Three rows of pinholes, each consisting of 86 circular orifices, 1 mm in diameter and equally separated by 1 mm, were made upstream of and parallel to the upper edge of the rear window and the upper and lower edges of the base, respectively. Smoke generated from paraffin oil was pumped through one hollow strut into the cavity in the rear part of the model and released from the pinholes to seed flow. Flow images were taken in the (y, z) plane at $x^* = 1.4$ in the wake.

2.3. *Aerodynamic drag and surface pressure measurements*

Time-averaged drag force was measured using a six-component aerodynamic force balance, which is accurate to 0.01 N. The balance was mounted on a rigid frame fixed directly onto the ground surface in order to minimize the effect of wind tunnel vibration on measurements (figure 2*a*). The test model was mounted on the balance using four hollow cylindrical posts of 280 mm in height and 15 mm in diameter made of rigid acrylic, which were fixed to a horizontal connecting plate that was screwed onto the balance. The connecting plate is a lightweight and rigid acrylic plate of 0.300 m × 0.220 m × 0.015 m, with a 0.08-m separation from the bottom wall of the test section. The posts were isolated from the raised floor or the wind tunnel wall to avoid possible force transmission. A sealed compartment was installed in the gap between the raised floor and the bottom wall of the test section, enclosing the four supporting posts, so that the posts were not subjected to the aerodynamic forces of the gap flow. The sampling frequency was 1 kHz, and the duration was 1 minute, producing a total of 6×10^4 data for each record. At least three records were collected for each test configuration.

The measured drag was corrected for the thrust forces generated by blowing using a method proposed by Littlewood & Passmore (2012). The thrust force F_j in the streamwise direction induced by the blowing jets was obtained at $U_\infty = 0$ m/s and then subtracted from the measured drag force on the model in an incident flow. The aerodynamic drag F_D is determined by

$$F_D = F_x - F_j, \tag{2.8}$$

where F_x is the drag force measured by the aerodynamic force balance. Then, the drag coefficient C_D is estimated by

$$C_D = \frac{F_D}{0.5\,\rho_{\text{air}}\,U_\infty^2\,A}. \tag{2.9}$$

The drag coefficient variation ΔC_D is calculated by

$$\Delta C_D = \frac{C_D - C_{D0}}{C_{D0}}, \tag{2.10}$$

where C_{D0} is the drag coefficient of the model in the absence of control.

A PSI DTC Initium system was used to monitor the time-averaged surface pressure on the model. Nineteen pressure taps were made, whose locations are schematically shown in figure 5. The time-averaged pressure coefficient C_{pi} is given by

$$C_{pi} = \frac{p_i - p_0}{0.5\,\rho_{\mathrm{air}}\,U_\infty^2},\ i \in \{1, 2, 3, \ldots, \text{or } 19\} \tag{2.11}$$

where p_i and p_0 are the local and free-stream static pressures, respectively. C_{p1} is measured at the center of the frontal face or the forward stagnation point of the Ahmed body. The $C_{p2} \sim C_{p5}$ measured in the symmetry plane of the rear window are well correlated with the flow separation over the slanted surface (Aubrun *et al.* 2011). The $C_{p11} \sim C_{p14}$ measured near the side edge ($y^* = 0.45$), which are sensitive to the change of the C-pillar vortices, contain information on how effective the C-pillar vortices are altered (Brunn *et al.* 2007). The $C_{p6} \sim C_{p10}$ and $C_{p15} \sim C_{p19}$ measured at the centerline and near the side edge of the vertical base, i.e. $y^* = 0$ and $y^* = 0.45$, are connected to the alternate emanation of coherent structures from the upper and lower recirculation bubbles behind the vertical base and the flow separation at the side edge of the base, respectively (Zhang *et al.* 2015). They are captured to monitor the base pressure change. The pressure taps are connected to an electronically scanned pressure (ESP) scanner using the plastic tubes of 1 mm in the inner diameter. The scanner is placed inside the body to minimize the length of the tubes connected to each tap and hence to limit the filtering effect of tubing in pressure measurements (Grandemange *et al.* 2013). The measurement accuracy is estimated to be ±3 Pa. At least three test runs were conducted for each measurement location. The sampling duration is 50 sec and f_s is 650 Hz. Define ΔC_{pi} by

$$\Delta C_{pi} = \frac{C_{pi} - C_{pi0}}{\left|C_{pi0}\right|}, \tag{2.12}$$

where C_{pi0} is the pressure coefficient in the base flow. Use $\langle C_p \rangle$ to denote the spatially averaged pressure coefficient of $C_{p2} \sim C_{p19}$ measured over the rear window and vertical base of the model. Then, the variation of $\langle C_p \rangle$ is given by

$$\Delta \langle C_p \rangle = \frac{\langle C_p \rangle - \langle C_{p0} \rangle}{\left|\langle C_{p0} \rangle\right|}, \tag{2.13}$$

where $\langle C_{p0} \rangle$ is the spatially averaged pressure coefficient for the uncontrolled flow.

The aerodynamic drag measurements were carried out at $U_\infty = 8 \sim 24$ m/s, corresponding to $Re = (0.9 \sim 2.7) \times 10^5$, and all other measurements were performed at $U_\infty = 15$ m/s ($Re = 1.7 \times 10^5$). Both Reynolds number Re and Strouhal number St are based on $\sqrt{A}$ and U_∞.

3. Results and discussion

3.1. *Characterization of the base flow*

The uncontrolled or base flow around the Ahmed body is first documented. The drag coefficient *CD0* exhibits a slight decrease from 0.38 to 0.35 as *Re* varies from 0.9×10^5 to 2.7×10^5 (figure 6). The uncertainty of the drag coefficient is estimated to be between 0.0004 and 0.003, i.e. at least one order of magnitude smaller than the drop (0.03) of *CD0*, as shown in figure 6. The measured drag and its variation agree well with previous studies (Aubrun *et al.* 2011, Thacker *et al.* 2012, Joseph *et al.* 2012). Thacker *et al.* (2012) measured using the force balance a decrease in *CD0* of an Ahmed model (= φ25°) from about 0.41 to 0.38 as *Re* was changed from 0.2×10^6 to 1.2×10^6. Their measurement uncertainty, estimated based on the accuracy (0.16 N) of the force balance, is between 0.0008 and 0.025, depending on *Re*; the higher end is one order of magnitude larger than ours (0.0004 ~ 0.003). The present small uncertainty is due to the higher resolution, 0.01 N, of the force balance.

The time-averaged velocity vectors and corresponding sectional streamlines (figure 7*a*,*b*) in the symmetry plane show a downwash flow from the rear window. For simplicity, sectional streamlines are hereinafter referred to streamlines. Unless otherwise stated, the reference frame for the streamlines is fixed on the ground. The result is consistent with Ahmed *et al.*'s (1984) observation based on the cross-flow velocity measurement at $x^* = 0.24$, 0.60 and 1.49 behind the vertical base of an Ahmed model (= φ 25°). They found that one pair of counter-rotating trailing vortices were formed in the wake, inducing a downwash flow in the central region of the wake. The pair of trailing vortices result from the interaction and downstream merging between the C-pillar vortices and the upper recirculation bubble behind the base (Zhang *et al.* 2015). The trailing vortices are quasi-streamwise and their centers occur off the centerline behind the base. As such, the trailing vortices are hardly discernible in the symmetry plane of the wake. The flow separated from the upper and lower edges of the base and then rolled up, forming two recirculation flow regions, one above the other, immediately behind the base, as highlighted by thick solid and dotted contours, respectively (figure 7*b*). The streamlines may allow us to determine the length of the recirculation flow region, defined by the maximum longitudinal length of region of $\overline{U} \leq 0$. As illustrated in figure 7(*b*), the lengths are $0.55\sqrt{A}$ and $0.53\sqrt{A}$ for the upper and lower recirculation regions, respectively. One saddle point, marked by symbol '×', occurs behind the recirculation regions. The upper and lower regions are characterized by negative and positive $\overline{\omega_y^*}$-contours (figure 7*c*), respectively.

The time-averaged velocity vectors and corresponding streamlines in the (*y*, *z*) plane of $x^* = 0.2$ (figure 8*a*,*b*) display four foci. The two foci that occur near the upper corners of the base coincide with the pair of large concentrations in the $\overline{\omega_x^*}$-contours (figure 8*c*) and are apparently due to the occurrence of the two counter-rotating C-pillar vortices. The other two at $y^* = \pm 0.22$ and $z^* = 0.23$

are associated with the trailing legs of the upper recirculation bubble behind the base. The ‘legs’ refer to the structures near the two lateral sides of the bubble. Ahmed *et al.* (1984) pointed out that the upper and lower recirculation bubbles behind the base resulted from two horseshoe vortices, located one above the other, and the trailing legs of the upper bubble were aligned longitudinally and merged with the C-pillar vortex. This observation is confirmed by Venning *et al.* (2017) in the study of the Ahmed-body wake (φ = 25°). As shown in the $\overline{\omega_x^*}$-contours in figure 8(*c*), the two most highly concentrated longitudinal vortices with a maximum magnitude of 13 in $\overline{\omega_x^*}$, marked by "C", are the well-known C-pillar vortices. There appears one $\overline{\omega_x^*}$ concentration in the vicinity of each C-pillar vortex with an opposite sign to that of the C-pillar vortex, and its maximum magnitude reaches about 2, which is induced by the C-pillar vortex (Zhang *et al.* 2015).

The PIV measurements were also conducted in a non-symmetry plane (y^* = 0.45) in order to gain insight into the three dimensionality of the unsteady structures in the wake. The streamlines of velocity vectors (figure 8*d*,*e*) display two foci behind the vertical base, which are connected to the upper and lower recirculation bubbles behind the base. The two structures are also reflected in the $\overline{\omega_y^*}$-contours (figure 8*f*), which display the negative and positive concentrations behind the base. On the other hand, there is one more pair of oppositely signed $\overline{\omega_y^*}$ concentrations, which occurs at the same height of the C-pillar vortices (figure 8*c*). As illustrated schematically in figure 9, the C-pillar vortices are generated from the shear layer rollup about the side edge of the rear window due to the pressure difference between the flow coming off the side surface and that over the rear window (Ahmed *et al.* 1984). This rollup motion may take the side vortices, originating from the recirculation bubble formed near the leading edge of the side surface (Zhang *et al.* 2015), with it, as illustrated by the structures marked by ‘J_1’, ‘J_2’ and ‘J_3’. However, the side vortices may retain their identity. When viewed in the (x, z) plane of y^* = 0.45, the rotating direction of structure J_1 located above the center of the C-pillar vortex is clockwise, while that of structures J_2 and J_3 below the C-pillar vortex center is anti-clockwise. The signs are consistent with the observed $\overline{\omega_y^*}$ concentrations. It may be inferred that the two oppositely signed $\overline{\omega_y^*}$ concentrations in the (x, z) plane of y^* = 0.45 (figure 8*f*) are the signature of the side vortices wrapping around the C-pillar vortex.

3.2. *Considerations for the deployment of actuations*

Most of previous investigations deployed a single actuator, for instance, blowing along the upper edge (e.g. Aubrun *et al.* 2011) or the two sides (Bruneau *et al.* 2011) of the window. It would be difficult for such actuation to alter effectively all three predominant coherent structures (Choi *et al.* 2014) for the maximum DR. For example, while blowing at the two upper corners of the window may weaken the C-pillar vortices and hence reduce the drag, the over-weakened C-pillar vortices can adversely affect flow separation over the window, causing a drag increase (Brunn *et al.* 2007). As such, it is plausible to implement multiple or combined actuations should the optimal modification of and interaction between the three coherent structures be obtained to maximize DR. Attempts have been made to deploy the combined actuations. Wassen & Thiele (2010) applied blowing around the rear window and the base**.** However, as noted in Introduction, the control parameters were not optimized, resulting in rather limited DR.

In the present investigation, S_1 and S_2 are deployed along the upper and side edges of the rear window, respectively, whereas S_3 and S_4 are placed along the upper and lower edges of the base, respectively (figure 3*a*). The S_1 has been demonstrated to be effective to suppress the flow separation from the upper edge of the window and to produce a pressure increase over the rear window (e.g. Aubrun *et al.* 2011). The S_2 can directly manipulate the shear layer rolling up about the side edge of the window, resulting in a weakened strength of the C-pillar vortices (Bruneau *et al.* 2011). The S_3 and S_4 can deflect the separated shear layer from the upper and lower base edges either upwards or downwards, depending on the blowing angles (Littlewood & Passmore 2012). These actuations are independent of each other and are optimized individually in terms of the blowing velocity and angle. Five different combinations, i.e. (S_1 and S_2), (S_3 and S_4), (S_1, S_2 and S_3), (S_1, S_2 and S_4) and (S_1, S_2, S_3 and S_4), are investigated to simultaneously control all the three types of structures for the maximized DR.

3.3. *DR and flow structure change under individual actuations*

Four individual actuations S_1, S_2, S_3 and S_4, based on steady blowing at different locations, are investigated for $Re = 1.7 \times 10^5$. The ensuing DR is discussed with the surface pressure coefficients measured on the rear window and the vertical base, along with the variation in the flow structure.

3.3.1. *Actuation S_1 along the upper edge of the rear window*

The dependence of C_D and ΔC_D on C_μ^{S1} is given in figure 10 as S_1 is operated at the blowing angles $\theta_{\mathrm{S1}} = 0°, 30°, 65°$ and $90°$. C_D and ΔC_D are apparently correlated to each other. There appear two critical momentum coefficients, $C_{\mu,\mathrm{c1}}^{\mathrm{S1}}$ and $C_{\mu,\mathrm{c2}}^{\mathrm{S1}}$, for each θ_{S1}. C_D rises initially with increasing C_μ^{S1} given $C_\mu^{\mathrm{S1}} \leq C_{\mu,\mathrm{c1}}^{\mathrm{S1}}$, due to an increased separation region over the slanted surface at small C_μ^{S1}, which results in a pressure drop over the slanted surface (Aubrun *et al.* 2011). Once C_μ^{S1} exceeds $C_{\mu,\mathrm{c1}}^{\mathrm{S1}}$, C_D drops, reaching the minimum at $C_\mu^{\mathrm{S1}} = C_{\mu,\mathrm{c2}}^{\mathrm{S1}}$ before rising again. The $C_{\mu,\mathrm{c2}}^{\mathrm{S1}}$ increases from 0.5×10^{-2} to 1.6×10^{-2} from $\theta_{\mathrm{S1}} = 0°$ to $90°$; meanwhile, the maximum DRs (figure 10*b*) are about 3%, 10%, 12% and 3% for $\theta_{\mathrm{S1}} = 0°, 30°, 65°$ and $90°$, respectively. A ΔC_D of -10% corresponds to a decrease in C_D by about 0.036 for $Re = 1.7 \times 10^5$. This result suggests that the optimal control is achieved at $\theta_{\mathrm{S1}} = 65°$, i.e. a blowing angle normal to the slanted surface. It will be shown later that the S_1 operated at this θ_{S1} produces a considerable alternation in the flow separation over the rear window and the upper and lower recirculation bubbles behind the base, accounting for the significant DR.

The variations in C_p on the rear window and the vertical base are compared in the vertical planes of $y^* = 0$ and 0.45 (figure 11*a*), which may provide insight into the flow physics behind the observed DR. In the measurement of C_p, the actuators were present in the uncontrolled flow, though not operated. The uncertainty of C_p is estimated to be within 0.01, corresponding to approximately 2% of the spatially averaged pressure coefficient (-0.43) of $C_{p2} \sim C_{p19}$. This averaged pressure is in good agreement with Lienhart and Becker's (2003) estimate (- 0.41) for an Ahmed body ($\varphi = 25°$, $Re = 8.9 \times 10^5$). When S_1 is operated at $C_\mu^{S1} = 1.1 \times 10^{-2}$ ($\theta_{S1} = 65°$), where the maximum DR by 12% is achieved, C_{p2} at $z^* = 0.81$ ($y^* = 0$) rises by 43%. However, the rise is rather mild downstream for C_{p3} (17%) and C_{p4} (6%), and even becomes indiscernible when approaching C_{p5}. At $y^* = 0.45$, C_{p11}, C_{p12}, C_{p13} and C_{p14} are increased by about 31%, 13%, 8% and 4%, respectively, as compared with their uncontrolled counterparts. Under control, flow separation is postponed downstream from the upper edge of the rear window, as will be shown later from the PIV data. This alternation is responsible for the overall recovery over the slanted surface. $C_{p6} \sim C_{p10}$ in the symmetry plane of the base increase but $C_{p15} \sim C_{p19}$ near the side edge drop, which are all linked to a change in the upper and lower recirculation bubbles, as will be shown later. An overall increase in the spatially averaged pressure by 12% is produced under S_1. It is worth pointing out that the variation in the averaged pressure is always approximately the same as the DR under control, be S_1, S_2, S_3, S_4 or their combinations.

C_{p1} measured at the center of the frontal face is about 1.0 with and without control. Similar observations have also been made for actuations S_2, S_3 and S_4. The altered time-averaged flow structures under S_1 is examined based on PIV measurements in an effort to unveil the DR mechanisms. Figure 11(*b*) presents the time-averaged streamlines measured in the symmetry plane under S_1 of $\theta_{S1} = 65°$ at the optimal C_μ^{S1} ($= 1.1 \times 10^{-2}$). A number of observations can be made from a comparison between the flows with and without control (figure 7*b*).

Firstly, flow separation under S_1 does not occur at the upper edge of the rear window anymore and is instead shifted downstream to $x^* \approx -0.24$, which is highlighted by a thick-contour circle, in distinct contrast to the base flow (figure 7*b*) where the flow remains attached over the rear window. This is not unexpected since the microjet array of S_1 generates streamwise vortices (e.g. Kuma & Alvi 2006). These vortices entrain higher momentum free-stream fluid to the near-wall low momentum region, which energizes the boundary layer fluid and prevents or delays flow separation. Furthermore, the separated shear layer appears joining the upper recirculation bubble behind the vertical base, that is, the flow separation region over the rear window becomes part of the recirculation bubble behind the base. As a result, there is a moderate pressure rise, by 6%, in C_{p4} at the center of the rear window (figure 11*a*).

The upper and lower recirculation bubbles are enlarged longitudinally under S_1 (figure 11*b*). To facilitate data interpretation, the bubbles, centers and saddle point shown in figure 7(*b*) are indicated by a broken curve and symbols '+' and '×' in red color, respectively. The center of the upper recirculation bubble under control appears shifting downstream and upward, relatively to the base flow. The center of the lower recirculation bubble and the saddle point also shift downstream. The sizes and centers of the recirculation bubbles are found to be closely connected to the surface pressure on the vertical base and hence the drag of the model (e.g. Pastoor *et al.* 2008; Metka & Gregory 2015; Rossitto *et al.* 2016). This connection is evident in the variation in C_p on the vertical base (figure 11*a*). The C_p displays a minimum, -0.32, at the position of C_{p8} ($z^* = 0.29$) in the uncontrolled flow. This minimum occurs at nearly the same height as that ($z^* = 0.27$) of the upper recirculation bubble center (figure 11*b*), apparently resulting from its proximity to this center. The center of the upper bubble moves downstream from $x^* = 0.12$ to 0.38 under control, causing a rise in C_{p8} by 22%. At the same time, this center goes up from $z^* = 0.27$ to 0.41 (figure 11*b*); the minimum C_p on the base moves to C_{p6} at $z^* = 0.41$ (figure 11*a*), again at the same height of the bubble center. This observation reinforces the conception that the location of the recirculation bubble center has a considerable effect on the base pressure.

In view of the highly three-dimensional (3D) flow, the altered flow structure under control is examined in the (y, z) plane of $x^* = 0.2$. Under S_1, the maximum concentration of $\overline{\omega_x^*}$ on each side of the rear window (figure 11*c*), which corresponds to the C-pillar vortex marked by "C", reaches about 12, almost the same as that (13) in the base flow (figure 8*c*). This result indicates that the actuation fails to weaken appreciably the C-pillar vortices. Further, the time-averaged streamlines (figure 11*c*) display two foci at (y^*, z^*) = (-0.38, 0.35) and (-0.45, 0.12), which are connected to the legs of the upper and lower recirculation bubbles, respectively. It appears that the upper and lower recirculation bubbles under S_1 tilt upstream toward the vertical base near the side edge of the base, as suggested by the anti-clockwise and clockwise rotational motions around the upper and lower foci, respectively. In comparison, the streamlines in the (y, z) plane of $x^* = 0.2$ show only one pair of foci at $y^* = \pm 0.22$ and $z^* = 0.25$ behind the base in the uncontrolled flow (figure 8*b*), corresponding to the trailing legs of the upper recirculation bubble. The modifications in the two bubbles account for the drop in $C_{p15} \sim C_{p19}$ near the side edge of the base (figure 11*a*).

The effectiveness of a steady slot jet (0.8 mm in width and 138 mm in length) arranged at the same position of S_1 is also examined. This actuation is referred to as S_1^{slot}. The blowing direction is normal to the rear window, the same as S_1 ($\theta_{S1} = 65°$). Such actuation leads to an increase in drag by 11% (not shown), in distinct contrast to the maximum DR of 12% under S_1 (figure 10*b*). The difference between S_1^{slot} and S_1 is ascribed to a difference in the jet exit shape. The rectangular slot produces a quasi-2D blowing jet, while the microjet array generates 3D streamwise vortices (e.g.

Johnston & Nishi 1990; Yang & Zhou 2016). The streamwise vortices enhance cross-stream mixing of streamwise momentum and hence suppress flow separation from the upper edge of the rear window, as supported by the PIV data (figure 11*b*).

3.3.2. *Actuation S_2 along the two side edges of the rear window*

As S_2 is operated at $\theta_{S2} = 30°$, C_D displays a slight drop initially with increasing C_μ^{S2} but grows continuously once C_μ^{S2} exceeds 0.2×10^{-2} (figure 12). The C_D drops slowly at $\theta_{S2} = 60°$ with increasing C_μ^{S2} but more rapidly at $\theta_{S2} = 90°$, with ΔC_D reaching -6% at $C_\mu^{S2} = 0.7 \times 10^{-2}$. The observation implies that S_2 may be more effective in increasing the swirl of the C-pillar vortices when directed normally to the slanted surface. The increasing swirl may act to propel the C-pillar vortices away to get diffused, causing a decrease in their strength (Bruneau *et al.* 2011).

The deployment of S_2 ($\theta_{S2} = 90°$) does not produce any marked change in the surface pressure over the rear window or at the vertical base. At $C_\mu^{S2} = 0.7 \times 10^{-2}$, the highest magnitude of the $\overline{\omega_x^*}$ concentration for the C-pillar vortices in the PIV measured $\overline{\omega_x^*}$-contours in the (y, z) plane of $x^* = 0.2$ is reduced to 10 (not shown), compared with that (13) in the base flow (figure 8*c*). As a result, C_{p11}, C_{p12}, C_{p13} and C_{p14} near the side edge of the rear window under control rise by 8%, 7%, 4% and 4%, respectively, which are ascribed to the weakened strength of the C-pillar vortices. On the other hand, the $C_{p2} \sim C_{p5}$ in the symmetry plane of the slanted surface, and $C_{p6} \sim C_{p10}$ and $C_{p15} \sim C_{p21}$ at the base change little under control.

It is worth mentioning that two arrays of steady circular microjets, denoted as S_2^{microjet}, directed normally to the slanted surface were used to replace S_2. The exit diameter of and separation between the orifices are the same as S_1. The maximum DR obtained is very small, only about 1% (not shown), that is, the slot jets are more effective than the microjet arrays in manipulating the C-pillar vortices.

3.3.3. *Actuation S_3 along the upper edge of the vertical base*

The effect of S_3 on ΔC_D is examined for five different blowing angles θ_{S3}. At $\theta_{S3} > 0$, C_D decreases with increasing C_μ^{S3} (figure 13*a*), ΔC_D reaching - 11% and - 7% at $C_\mu^{S3} = 6.9 \times 10^{-2}$ for $\theta_{S3} = 45°$and 30° (figure 13*b*), respectively. At $\theta_{S3} = 0°$, the drag is slightly increased. For $\theta_{S3} < 0°$, however, ΔC_D continuously rises with increasing C_μ^{S3}, reaching 11% and 20% at $\theta_{S3} = -30°$ and $-45°$ ($C_\mu^{S3} = 6.9 \times 10^{-2}$), respectively.

At $C_\mu^{S3} = 6.9 \times 10^{-2}$ ($\theta_{S3} = 45°$) where the maximum DR of 11% is produced, C_{p2} increases by 27% in the plane of symmetry (figure 14*a*). The pressure rise contracts downstream, ΔC_{p3}, ΔC_{p4} and ΔC_{p5} being 10%, 4% and 2%, respectively. Similar observation is made near the side edge of the rear window, where C_{p11}, C_{p12}, C_{p13} and C_{p14} rise by 25%, 5%, 4% and 4%, respectively. It is interesting to note that S_3, though deployed along the upper edge of the vertical base, has a great influence on the surface pressure over the rear window, implying an upstream effect on the flow structure over the slanted surface. S_3 acts to increase $C_{p6} \sim C_{p10}$ in the symmetry plane of the base on one hand but to decrease $C_{p15} \sim C_{p19}$ near the side edge on the other hand. It will be later shown that S_3 incurs a marked change in the flow structure over the rear window and behind the vertical base, which accounts for the pressure variation.

Under this control, flow separation occurs downstream of the upper edge of the rear window and the separated flow reattaches on the slanted surface, forming a separation bubble (figure 14*b*). Its size is greatly larger than that of the small separation bubble formed near the upper edge of the rear window in the base flow (figure 7*b*). Furthermore, the separated shear layer from the upper edge of the base is deflected upwards by S_3, and the upper and lower recirculation bubbles are longitudinally more stretched than the non-controlled case. Meanwhile, the centers of the two bubbles, as well as the saddle point, are pushed downstream. It is therefore plausible that the pressure rise of C_{p8} at the center of the base by 31% is due to the modifications in the upper and lower recirculation bubbles behind the base.

The flow structure in the (y, z) plane of $x^* = 0.2$ (figure 14*c*) exhibits a number of changes under control as compared with the uncontrolled flow (figure 8*b*,*c*). Firstly, the maximum magnitude of the $\overline{\omega_x^*}$ concentration associated with the C-pillar vortex is only 8, significantly lower than that (13) in the uncontrolled flow (figure 8*c*), that is, the C-pillar vortex is weakened substantially in strength. Secondly, the streamlines (figure 14*c*) show two foci, one at (y^*, z^*) = (-0.38, 0.47) and the other at (y^*, z^*) = (-0.38, 0.11), behind the base, which correspond to the legs of the upper and lower recirculation bubbles, respectively. Note that $C_{p15} \sim C_{p19}$ decrease under S_3, as the case under S_1 (figure 11*a*, *c*). It may be inferred that the drop in $C_{p15} \sim C_{p19}$ under S_3 is due to the proximity to the centers of the upper and lower recirculation bubbles.

At $C_\mu^{S3} = 6.9 \times 10^{-2}$ and $\theta_{S3} = -45°$, S_3 leads to a drag increase by about 20% (figure 13*b*). The time-averaged streamlines (not shown) show that the shear layer, when separated from the upper edge of the base, is deflected downwards by the blowing but, when separated from the lower edge, sweeps towards the ground without rolling up, resulting in only one recirculation bubble. This bubble expands downwards, though shrinking longitudinally, compared with the upper recirculation bubble in the base flow; meanwhile, the center of the bubble is shifted closer to the base, accounting for the drag increase at negative θ_{S3}.

3.3.4. *Actuation S_4 along the lower edge of the vertical base*

With increasing C_μ^{S4}, C_D decreases (figure 15*a*) and ΔC_D is negatively more pronounced, down to -14% at $C_\mu^{S4} = 6.9 \times 10^{-2}$ for $\theta_{S4} = 45°$ (figure 15*b*) but only - 2% for $\theta_{S4} = 30°$. At this C_μ^{S4} ($\theta_{S4} = 45°$), C_{p2} is increased by 28% relatively to the uncontrolled flow (figure 16*a*). Further downstream,

C_{p3}, C_{p4} and C_{p5} rise by 14%, 6% and 2%, respectively. At $y^* = 0.45$, C_{p11}, C_{p12}, C_{p13} and C_{p14} go up by 26%, 9%, 6% and 6%, respectively. The results indicate that, like S_3, S_4 produces an effect on the flow structure over the rear window. $C_{p11} \sim C_{p14}$ on the base ($y^* = 0$) rise but $C_{p15} \sim C_{p19}$ ($y^* = 0.45$) drop under S_4. Once $\theta_{S4} \leq 0°$, ΔC_D turns to the opposite (figure 15*b*), reaching 8% and 15% at $C_\mu^{S4} = 6.9 \times 10^{-2}$ for $\theta_{S4} = -30°$ and -45°, respectively.

Several changes take place with the flow structure under S_4 operated at $C_\mu^{S4} = 6.9 \times 10^{-2}$ and $\theta_{S4} = 45°$. Similarly to the case of S_3 at $\theta_{S3} = 45°$, the streamlines (figure 16*b*) display an enlarged separation bubble over the rear window, and longitudinally expanded upper and lower recirculation bubbles behind the base, as compared with the uncontrolled flow. One saddle point occurs above the upper edge of the base, which probably results from the interaction between the downwash flow reattaching on the slanted surface and the upwash flow near the upper edge of the base. Due to the change in the flow structure, C_{p4} and C_{p8} measured at the centers of the rear window and vertical base recover by about 6% and 30% (figure 16*a*), respectively. Meanwhile, the strength of C-pillar vortices is substantially reduced (figure 16*c*). Furthermore, the pair of foci at $y^* = \pm\, 0.22$ and $z^* = 0.23$ shown in the streamlines (figure 8*b*), which are connected to the trailing legs of the upper recirculation bubble, cannot be observed anymore under S_4 (figure 16*c*), suggesting a change in the upper recirculation bubble. In fact, the streamlines in the (x, z) plane of $y^* = 0.45$ (not shown) display two centers, one above the other, behind the base, which are associated with the upper and lower recirculation bubbles, respectively. The upper center occurs at $x^* = 0.33$ and $z^* = 0.43$, almost the same as that ($x^* = 0.33$, $z^* = 0.45$) in the symmetry plane of the wake (figure 16*b*), suggesting that the legs of the upper bubble are horizontally orientated and parallel to the vertical base of the model. Due to the change in the flow structure, $C_{p15} \sim C_{p19}$ measured near the side edge of the base decrease by 3% ~ 30%.

The effect of Re on the DR for S_1, S_2, S_3 and S_4 at different blowing angles is examined at $Re = 1.3 \times 10^5$, 1.7×10^5 and 2.0×10^5. Under each actuation, the dependence of ΔC_D on the momentum coefficient is mostly the same for the three different *Re*s. This is not unexpected. The flow separation lines are fixed at the sharp edges of the rear window and the vertical base of the Ahmed body. Nevertheless, a difference in ΔC_D is appreciable under S_2 ($\theta_{S2} = 90°$) as Re varies. The optimal C_μ^{S2} is 0.7×10^{-2} at $Re = (1.7 \sim 2.0) \times 10^5$, which is smaller than that (1.2×10^{-2}) at $Re = 1.3 \times 10^5$ (not shown). A smaller Re is associated with an increase in the separation region and hence a larger low-pressure area on the rear window in the absence of control (Joseph *et al.* 2012), which is confirmed by an increase in C_D from 0.35 to 0.37 as Re drops from 2.0×10^5 to 1.3×10^5 (figure 6). As a result, the pressure difference between flows on the rear window and the side surface is augmented, producing an increased strength in the C-pillar vortices. As such, a larger C_μ^{S2} is required to break the C-pillar vortices at $Re = 1.3 \times 10^5$, as compared with the higher Re. A difference in ΔC_D is also discernible under S_1 at $\theta_{S1} = 65°$ once $C_\mu^{S1} \geq 1.1 \times 10^{-2}$ (not shown). As under S_2 ($\theta_{S2} = 90°$), the optimal C_μ^{S1} is higher for larger Re. That is, the observed Re effects are mainly due to the Re dependence of the flow separation bubble on the slanted surface.

3.3.5. *Unsteady structures emanated from the two recirculation bubbles behind the base*

E_u (figure 17*a*) of u_{xz} measured at location W ($x^* = 0.4$, $y^* = 0$, $z^* = 0.18$) displays a peak at $f^* = 0.52$ without control ($C_\mu^{S1} = 0$). This peak results from the alternate emanation of structures from the upper and lower recirculation bubbles behind the base. Under the actuation of S_1 ($\theta_{S1} = 65°$) this peak remains pronounced at $C_\mu^{S1} = 0.1 \times 10^{-2}$ and 0.2×10^{-2} but retreats at $C_\mu^{S1} = 0.4 \times 10^{-2}$. The peak at $f^* = 0.52$ in E_u vanishes as C_μ^{S1} is further increased, implying that the alternate emanation of structures is interrupted by the control. Note that at this C_μ^{S1}, C_{p8} at the center of the base increases by about 22% (figure 11*a*) and drag reduces by 12% (figure 10*b*). This result indicates that the alternately emanated structures from the two bubbles are closely connected to the base pressure and hence the aerodynamic drag of the Ahmed body. Zhang *et al.* (2015) further found that the recirculation bubbles were characterized by periodic enlargement and contraction, and the coherent structures were alternately emanated from the two bubbles. They proposed that the bubble, be it upper or lower, expanded in size as a result of entrainment of the separated flow, which caused a gradual rise in pressure within the bubble. The bubble eventually burst when the pressure reached a certain level, accompanied with a substantially reduced size of the bubble and a structure emanated from it. At the same time, the other bubble continued its rise in size and pressure until its collapse, associated with a downsize and the emanation of a structure from it. However, under control, an increase in the size of the two recirculation bubbles implies relatively more stagnant fluid within the bubbles. As a result, the dynamic process of the bubble growth and burst is interrupted and even suppressed, which is corroborated by the disappearance of the alternate emanation of the coherent structures from the two bubbles.

The peak at $f^* = 0.52$ in E_u is discernible under S_2 at $\theta_{S2} = 90°$, regardless of the momentum coefficient value (figure 17*b*). Apparently, the actuation fails to break the organized structures. The corresponding DR is rather limited, around 6% (figure 12*b*). When S_3 is operated at $\theta_{S3} = 45°$, the peak at $f^* = 0.52$ in E_u remains discernible up to $C_\mu^{S3} = 0.1 \times 10^{-2}$ but appears weaker at $C_\mu^{S3} = 0.8 \times 10^{-2}$ and disappears at $C_\mu^{S3} \geq 1.9 \times 10^{-2}$ (figure 17*c*). Similarly, under S_4 at $\theta_{S4} = 45°$, the E_u (figure 17*d*) displays a peak at $f^* = 0.52$, which becomes weak and then vanishes from $C_\mu^{S4} = 0.1 \times 10^{-2}$ to 4.6×10^{-2}. The disappearance of the alternately emanated structures from the two recirculation bubbles under S_3 or S_4 leads to a significant reduction in drag by 10% and 12% at the momentum coefficient of 4.6 × 10^{-2} (figures 13*b* and 15*b*), respectively.

The effect of the blowing angle on the unsteady structure of $St = 0.52$ is investigated. The results are summarized in figure 18. A number of observations can be made. Firstly, S_1 is effective in breaking up the unsteady structures of $St = 0.52$ at $\theta_{S1} = 90°$, as at $\theta_{S1} = 65°$, given an adequately large C_μ^{S1}, but not at $\theta_{S1} = 0°$ and 30°. Secondly, although ineffective at $\theta_{S2} = 60°$ and 90°, S_2 at $\theta_{S2} = 30°$ may eradicate the structures provided $C_\mu^{S2} \geq 1.6 \times 10^{-2}$. Thirdly, S_3 at $\theta_{S3} = 45°$ is effective in eradicating the unsteady structures given $C_\mu^{S3} \geq 1.9 \times 10^{-2}$ as the two bubbles behind the base are considerably enlarged (figure 14*b*). So does S_3 at $\theta_{S3} = -45°$ for very large C_μ^{S3} ($\geq 3.5 \times 10^{-2}$), though the physics behind is different, the upper bubble shrinks greatly. Finally, S_4 may effectively destroy the structures at positive θ_{S4} (figure 16*b*), but not at $\theta_{S4} \leq 0°$.

3.4. *Combined actuations*

3.4.1. *Control performance*

As documented in detail by Zhang *et al.* (2015), the Ahmed body wake is highly complicated and characterized by distinct organized motions such as the C-pillar vortices, separation bubble over the rear window, two recirculation bubbles behind the base, alternately emanated structures from the two bubbles. Furthermore, these organized structures are coupled, that is, manipulating one may affect another or more. Consequently, while suppressing one or two organized structures and associated drag, the actuation may alter another structure, which contributes to a rise in drag (Brunn *et al.* 2007). Naturally, individual actuations S_1, S_2, S_3 and S_4, each manipulating one or two types of organized structures, may have difficulty in control effectively all or most of the organized structures and thus achieve only rather limited DR, as demonstrated in § 3.3. One issue arises, that is, can we find a technique that combines the individual actuations to manipulate all or most of the organized structures for a significantly better control performance? In this section, we explore different combinations of individual actuations to maximize DR at $Re = 1.7 \times 10^5$. Three schemes will be examined, i.e. combinations of S_1 and S_2, S_3 and S_4, and S_1, S_2, S_3 and S_4. S_1 and S_2 are directed normally to the slanted surface, i.e. $\theta_{S1} = 65°$ and $\theta_{S2} = 90°$, and S_3 and S_4 are operated at $\theta_{S3} = \theta_{S4} = 45°$. Such orientations, along with the fact that each actuation has its own independent air passage/chamber, lead to little interference between individual actuations.

As presented in §3.3, S_1 may produce three effects, i.e. the downstream shift of the flow separation from the upper edge of the rear window, the longitudinal enlargement of the upper and lower recirculation bubbles, and the interruption of the alternate emanation of structures from the two bubbles, thus resulting in a DR by 12%. On the other hand, S_2 suppresses largely only the C-pillar vortices, leading to a maximum DR by 6%. However, there exists a coupling between the C-pillar vortices and the separation bubble over the rear window (Brunn *et al.* 2007). In view of this, we deploy a combination of actuations S_1 and S_2 to control simultaneously the two types of structures. C_D and ΔC_D depend on C_μ^{S1} and C_μ^{S2}, as shown in figure 19 ($Re = 1.7 \times 10^5$). Their experimental uncertainties are estimated to be less than 0.003 and 0.7%, respectively. The combined S_1 and S_2 always lead to DRs. The C_D drops substantially compared with the uncontrolled flow. Two local maxima occur, one at (C_μ^{S1}, C_μ^{S2}) = (0.3×10^{-2}, 2.0×10^{-2}) and the other at (1.2×10^{-2}, 1.3×10^{-2}), reaching 16% and 14% (figure 19*b*), respectively. The former exceeds any previously reported DR using active techniques (table 1), where the maximum DR obtained is 14% (Aubrun *et al.* 2014). Evidently, the overly large C_μ^{S1} and C_μ^{S2} may lead to a deteriorated control performance. The changes in the flow structure under this combined actuation will be discussed later based on the surface pressure data.

At $C_\mu^{S1} = 0.3 \times 10^{-2}$ and $C_\mu^{S2} = 2.0 \times 10^{-2}$, C_{p2}, C_{p3}, C_{p4} and C_{p5} at $y^* = 0$ are increased by about 39%, 19%, 10% and 2% (figure 19*c*), respectively. Note that the magnitude of ΔC_{p2} under combined S_1 and S_2 is smaller than that (43%) under S_1 (figure 11*a*). This is reasonable since the weakened C-pillar vortices under the combined S_1 and S_2 may lead to an increased flow separation over the rear window because the two structures are coupled. C_{p11}, C_{p12}, C_{p13} and C_{p14} near the side edge ($y^* = 0.45$) of the slanted surface also go up by 35%, 13%, 10% and 7%, respectively. The change in the upper and lower recirculation bubbles behind the base under this combined actuations bears a similarity to that under S_1 (figure 11*b*,*c*). The two bubbles expand longitudinally under control in the symmetry plane, which accounts for the rise in $C_{p6} \sim C_{p10}$ on the base at $y^* = 0$. Near the side edge of the base, the legs of the two bubbles are tilted upstream toward the base due to control, leading to a decrease in $C_{p15} \sim C_{p19}$ at $y^* = 0.45$, which are in close proximity to the center of the two bubbles. The averaged pressure over $C_{p2} \sim C_{p19}$ is increased by 15% under this combination.

No matter whether S_3 or S_4 is deployed at $\theta_{S3} = \theta_{S4} = 45°$, the substantial DR (figures 13 and 15) is associated with the suppression of the C-pillar vortices (figures 14*c* and 16*c*), the longitudinally enlarged recirculation bubbles behind the base (figures 14*b* and 16*b*), and the elimination of the alternate emanated structures from the two bubbles (figure 17*c*,*d*). When the two actuations are combined, the C_D reaches its minimum of about 0.30 at $C_\mu^{S3} = 8.2 \times 10^{-2}$ and $C_\mu^{S4} = 6.9 \times 10^{-2}$ (figure 20*a*), producing a maximum DR of 18% (figure 20*b*). Correspondingly, C_{p2} rises by 43% (figure 20*c*), higher than those (27% and 28%) produced under S_3 (figure 14*a*) and S_4 (figure 16*a*). Further downstream, C_{p3} and C_{p4} are increased by 22% and 10%, respectively, though C_{p5} near the lower edge of the slanted surface is almost unchanged. $C_{p11} \sim C_{p14}$ near the side edge of the rear window also rise by 7% ~ 40%. The $C_{p6} \sim C_{p10}$ and $C_{p15} \sim C_{p19}$ increase and decrease, respectively, relatively to the uncontrolled flow. Their average rises by 17% under control.

To enhance further the DR performance, the combination of S_1, S_2, S_3 and S_4 is deployed to control simultaneously the separation bubble and the C-pillar vortices over the rear window and the two recirculation bubbles behind the base. Under this scheme, C_μ^{S1} and C_μ^{S2} are set at 0.3×10^{-2} and 2.0×10^{-2}, respectively, at which a DR by 16% was obtained provided that S_1 and S_2 are simultaneously implemented. Figure 21(*a*, *b*) presents the contours of the dependence of C_D and ΔC_D on C_μ^{S3} and C_μ^{S4}. At $C_\mu^{\mathrm{S4}} = 0$, i.e. under the combination of S_1, S_2 and S_3, ΔC_D drops with increasing C_μ^{S3} and reaches the minimum, -25%, at $C_\mu^{\mathrm{S3}} = 5.6 \times 10^{-2}$, beyond which there is no further decrease in drag. On the other hand, at $C_\mu^{\mathrm{S3}} = 0$ or under the combination of S_1, S_2 and S_4, ΔC_D declines with increasing C_μ^{S4}, reaching the minimum, -26%, at $C_\mu^{\mathrm{S4}} = 8.2 \times 10^{-2}$, beyond which ΔC_D increases gradually for higher C_μ^{S4}. Finally, as S_1, S_2, S_3 and S_4 are all operated, a maximum reduction in drag by 29% is obtained at $C_\mu^{\mathrm{S3}} = 1.9 \times 10^{-2}$ and $C_\mu^{\mathrm{S4}} = 8.2 \times 10^{-2}$. This is higher than any previously reported DR and in fact very close to the target (30%) set by automotive industries (Bruneau *et al.* 2011). Under this combination, there is a large pressure recovery about the center of the rear window (figure 21*c*), ΔC_{p2}, ΔC_{p3}, ΔC_{p4} and ΔC_{p5} reaching 55%, 39%, 31% and 21%, respectively. It is worth noting that ΔC_{p5} is significantly larger than those (< 2%) under the four individual actuations and the two combined actuations (S_1 and S_2 or S_3 and S_4), as shown in figures 11(*a*), 14(*a*), 16(*a*), 19(*c*) and 20(*c*). It will be shown later that this marked pressure recovery is associated with the entrainment of control-generated coherent structures, formed near the lower end of the slanted surface, into the separation bubble over the rear window. On the other hand, C_{p11}, C_{p12}, C_{p13} and C_{p14} near the side edge of the rear window are increased by 45%, 27%, 23% and 22%, respectively. The $C_{p6} \sim C_{p10}$ about the symmetry plane of the base all rise by 23% ~ 38%, though $C_{p15} \sim C_{p19}$ near the side edge of the base are essentially the same as those in the uncontrolled flow. Overall, the averaged pressure rises by 28%.

Table 2 summarizes the maximum DRs and pressure recoveries on the rear window and the vertical base under the four individual actuations S_1, S_2, S_3 and S_4, and their combinations. The maximum reductions in drag produced by S_1, S_2, S_3 and S_4 are 12%, 6%, 11% and 14%, respectively. The combined actuations (S_1 and S_2), (S_3 and S_4), (S_1, S_2 and S_3) and (S_1, S_2 and S_4) produce DRs by 16%, 18%, 25% and 26%, respectively. The combined S_1, S_2, S_3 and S_4 achieves the highest reduction in drag.

3.4.2. *Altered flow structure*

This section is focused on the altered flow structure that corresponds to the maximum DR of 29%, with a view to understanding the DR mechanisms behind. Figure 22 presents the altered flow structure in the symmetry plane under the combination of S_1, S_2, S_3 and S_4, which yields the maximum

DR of 29%. The changes (figure 22*a*, *c*) in flow separation over the rear window and the two recirculation bubbles behind the base resemble those under the individual S1, S3 and S4 (figures 11*b*, 14*b* and 16*b*). Nevertheless, there are differences. Firstly, one strip of the positive $\overline{\omega_y^*}$ concentration is seen attaching to the rear window, with its highest magnitude reaching 5 (figure 22*b*). This positive vorticity strip is linked to the impressive increase in pressure on the rear window, by 31% in *Cp4* at the center (figure 21*c*). One scenario is proposed for the observations. Under the combined combination, especially S3 and S4, the two recirculation bubbles behind the base grow in size substantially, taking their centers downstream. The increased distance between the centers and the base acts to increase significantly the base pressure (figure 21*c*). Meanwhile, the separation bubble on the rear window and the upper recirculation bubble behind the base are connected or merge into one, as supported by figure 22 (cf. figure 7*b*), and then the higher base pressure than that on the window (figure 21*c*) produces an upward rollup (figure 22*c*,*d*), corresponding to the positive $\overline{\omega_y^*}$, accounting for the positive vorticity strip. With the two bubbles joining together, the significantly higher base pressure pushes up the pressure on the window, as noted in figure 21*c*.

The flow structure change under control is examined in the (*x*, *z*) plane of $y^* = 0.45$ in view of the highly 3D flow. The ω_y^*-contours in the base flow show two oppositely signed ω_y^* concentrations, enclosed by a thick contour in figure 23(*a*), behind the upper edge of the base. When the control is implemented, the occurrence of these ω_y^* concentrations is shifted upstream and upward (figure 23*b*), compared with the base flow (figure 23*a*). Furthermore, as shown in the $\overline{\omega_y^*}$-contours (figure 23*d*), both negative and positive vorticity concentrations, coinciding spatially with the C-pillar vortices, are impaired under control; their maximum magnitudes drop to 4 and 2, respectively, considerably lower than their counterparts (7, 11) in the base flow (figure 23*c*).

The weakened vorticity concentrations are connected to the greatly impaired C-pillar vortices under control. As shown in the $\overline{\omega_x^*}$-contours in the (*y*, *z*) plane of $x^* = 0.2$ (figure 24*a*), the maximum magnitude of the $\overline{\omega_x^*}$ concentration of the C-pillar vortices is about 6, less than one half of that (13) in the base flow (figure 8*c*). Note that the C-pillar vortices are formed by shear layer rolling up around the side edge of the rear window due to the pressure difference between the flow over the slanted surface and that coming off the side face of the model. Therefore, an overall increase in the surface pressure at the rear window under control (figure 21*c*) may decrease this pressure difference and hence lead to the weakened C-pillar vortices. On the other hand, the C-pillar vortex center, identified with the maximum vorticity concentration, occurs at $y^* = 0.42$ and $z^* = 0.69$, which is deflected upward and toward the symmetry plane, as compared with that ($y^* = 0.45$ and $z^* = 0.6$) in the base flow. The movement of the C-pillar vortex under control naturally causes the side vortices separated from the side edge of the rear window to shift upstream and upward, thus resulting in the upstream and upward shift in the two oppositely signed ω_y^* concentrations under control (figure 23*b*). Near the symmetry plane, the streamlines emanate from the center of the vertical base to the upper and lower edges of the base, which are associated with the upper and lower recirculation bubbles, respectively; please refer to the time-averaged streamlines in the (x, z) plane (figure 22*c*). Nevertheless, the two recirculation bubbles are hardly discernible from the streamlines in the (x, z) plane of $y^* = 0.45$ (figure 24*b*). The streamlines exhibit one node near $x^* = 0.15$ and $z^* = 0.4$. The flow about the node is highly 3D, with a velocity gradient in the y direction, as indicated by the streamlines in the (y, z) plane of $x^* = 0.2$ (figure 24*a*). The presence of the node is ascribed to the shear layers that sweep across this plane, indicating a transportation of fluid from the central region to the lateral side behind the base, which accounts for the 2% rise in the spatially averaged pressure coefficient of $C_{p15} \sim C_{p19}$ near the side edge of the base (figure 21*c*). The observation from the PIV data is also substantiated by flow visualization data in the (y, z) plane of $x^* = 1.4$. One pair of counter-rotating trailing vortices is evident in the base flow (figure 24*c*). The C-pillar vortex and the upper recirculation bubble interact with each other, and merge downstream, forming one pair of trailing vortices in the wake (Zhang *et al.* 2015). Under control, the trailing vortices cannot be observed anymore (figure 24*d*), implying greatly impaired or even eliminated vortices.

A conceptual model is proposed for the altered flow structure under the control of combined S_1, S_2, S_3 and S_4, which leads to a great reduction in drag, as sketched in figure 25. Compared with the uncontrolled flow, the flow separation point is shifted downstream, instead of being fixed at the upper edge of the rear window (figure 22*a*). The separated shear layer reattaches near the lower end of the rear window, forming a separation bubble. The downwash reattaching flow interacts with the upwash caused by blowing along the upper edge of the vertical base, producing a structure near the lower end of the slanted surface. This structure is then entrained into the separation bubble under the effect of recirculating flow over the rear window, which is responsible for the strip of positive vorticity concentrations attaching to the slanted surface (figure 22*b*). Similar observations have also been made for the combination of S_1, S_2 and S_3. In contrast, such a positive vorticity strip cannot be observed under S_3 or S_4, nor under their combination, in spite of the presence of a separation bubble over the rear window (figures 14*b* and 16*b*). Accordingly, ΔC_{p4} at the center of the slanted surface reach only 4%, 6% and 10% under S_3, S_4 and ($S_3 + S_4$), respectively, far less than those (25% and 31%) produced by the combinations of (S_1, S_2, and S_3) and (S_1, S_2, S_3 and S_4). It is therefore plausible that the entrainment of the control-generated structure into the separation bubble over the rear window may play a significant role for the pressure rise on the slanted surface. The C-pillar vortices are significantly weakened in strength under control (figure 24*a*) as compared with those in the base flow, leading to a large increase by 23% in C_{p13} measured near the side edge of the rear window (figure 21*c*). The side vortices, formed over the side surface of the body, are wrapped up around the side edge of the rear window under the rollup effect of the shear layer coming off the side surface along the slanted side edge (Zhang *et al.* 2015). This explains why there exist two oppositely signed ω_y^* concentrations, coinciding spatially with the C-pillar vortices, in the typical instantaneous ω_y^*-contours measured in (x, z) plane of $y^* = 0.45$ (figure 23*b*).

The streamlines (figure 22*c*) unveil that the upper and lower recirculation bubbles behind the base are expanded by more than 50% (cf. figure 7*b*), which is linked to the upward deflection of the separated shear layer from the upper edge of the base under S_3. This expansion is associated with a shift both downstream and upward in the center of the upper bubble and a downstream shift in the center of the lower bubble; meanwhile, the saddle point moves downstream. Furthermore, the alternate emanation of the coherent structures from the two bubbles disappears. Correspondingly, C_{p8} at the center of the vertical base recovers by 38% (figure 21*c*). One strip of positive vorticity concentrations attaches to the base, as is evidenced in $\overline{\omega_y^*}$-contours (figure 22*d*). In the uncontrolled flow, the C-pillar vortices and the upper recirculation bubble interact with each other, forming one pair of counter-rotating trailing vortices in the wake (figure 24*c*). However, the pair of trailing vortices disappear under control, as shown in the flow visualization data in the (y, z) plane of $x^* = 1.4$ (figure 24*d*). This is not unexpected in view of the weakened C-pillar vortices and the changes in the upper recirculation bubble behind the base.

3.5. *Control efficiency*

It is important to find out whether the developed control technique, though effective for producing DR, is efficient and whether the power saved due to the reduced aerodynamic drag is larger than the power input for producing actuation. To this end, we analyzed the experimental data obtained at $U_\infty = 15$ m/s, corresponding to $Re = 1.7 \times 10^5$.

The power to overcome aerodynamic drag on the model in the base flow case is given by

$$P_{D0} = F_{D0}\, U_\infty, \tag{3.1}$$

where F_{D0} is the aerodynamic drag of the model in the base flow. Following Aubrun *et al.* (2011), Littlewood & Passmore (2012) and Barros *et al.* (2016), the power saving due to a decrease in drag (ΔF_D) may be written as

$$\Delta P_D = \Delta F_D\, U_\infty. \tag{3.2}$$

The experimental uncertainty in the estimate of ΔP_D is given by $\overline{\left|\Delta F_D - \overline{\Delta F_D}\right|}\cdot U_\infty$, which is less than 0.15 W or 0.7% of P_{D0} for all cases. Following energy input analyses by, e.g. Wassen & Thiele (2010) and Barros *et al.* (2016), the power input under S_i may be calculated by

$$P_{Si} = 0.5 N_{\mathrm{Si}}\, \rho_{\mathrm{air}}\, Q_{\mathrm{Si}}\, V_{\mathrm{Si}}^2\,,\ i \in \{1, 2, 3 \text{ or } 4\}. \tag{3.3}$$

The control efficiency (η) is defined as the ratio of ΔP_D to total input power (e.g. Choi *et al.* 2008; Aubrun *et al.* 2011; Barros *et al.* 2016), viz.

$$\eta = \frac{\Delta P_D}{\sum_{i=1}^{4} P_{\mathrm{Si}}}. \tag{3.4}$$

The control is considered efficient when η is larger than unity.

Figure 26 shows the dependence of η on C_μ for individual S1 (θS1 = 65°), S2 (θS2 = 90°), S3 (θS3 = 45°) and S4 (θS4 = 45°). For all cases, the large η occurs at small momentum coefficient (figure 26*a*) or low jet exit velocity. At $C_\mu \approx 0.2 \times 10^{-2}$, η reaches about 37.5, 32.8, 16.1 and 8.4 under S1, S2, S3 and S4, respectively. Beyond this C_μ, η decreases continuously with increasing C_μ. The η remains efficient ($\eta > 1$) below C_μ of 1.3×10^{-2} (figure 26*c*). At this C_μ, the DRs are 11%, 3%, 6% and 6% under S1, S2, S3 and S4 (figures 10*b*, 12*b*, 13*b* and 15*b*), respectively. On the other hand, when C_μ goes above 2.2×10^{-2}, η becomes smaller than unity for every actuation, that is, the control input power is larger than the power saving from the DR.

The control efficiency is also assessed for different combinations, as listed in table 3. The uncertainty of η is calculated to be about 1.3 at $C_\mu \approx 0.1 \times 10^{-2}$, and below 0.1 as C_μ is increased above 0.7×10^{-2}. Under the combined S1 and S2, a relatively high η, about 34.3, is produced at $C_\mu^{\mathrm{S1}} = 0.2 \times 10^{-2}$ and $C_\mu^{\mathrm{S2}} = 0.1 \times 10^{-2}$, corresponding to a DR of 7% (figure 19*b*); η is 3.9, indicating an energy saving four times greater than the input energy at $C_\mu^{\mathrm{S1}} = 0.3 \times 10^{-2}$ and $C_\mu^{\mathrm{S2}} = 2.0 \times 10^{-2}$, where the maximum DR of 16% is obtained. For the combination of S3 and S4, η is less than unity although considerably high DRs can be achieved at high momentum coefficients. With all the four actuations combined ($C_\mu^{\mathrm{S1}} = 0.3 \times 10^{-2}$, $C_\mu^{\mathrm{S2}} = 2.0 \times 10^{-2}$), η reaches 4.4 at $C_\mu^{\mathrm{S3}} = C_\mu^{\mathrm{S4}} = 0.1 \times 10^{-2}$, corresponding to a DR of 18%. It is noteworthy that this DR is nearly the same as the maximum DR (18%) obtained under the combination of S3 and S4, but the corresponding η is much larger than that (0.15) for the latter. Similarly, the maximum DR (16%) and the resultant η (3.9) under the combination of S1 and S2 are also appreciably smaller than their counterparts (18% and 4.4) under the combined S1, S2, S3 and S4. In comparison, Wassen & Thiele (2008) achieved a η of 1.2 and a DR of 6% by deploying streamwise steady blowing around the rear window and the vertical base. By changing the directions of the blowing jets, Wassen & Thiele (2010) improved η to 1.7 and obtained a DR of 10%. Bruneau *et al.* (2011) deployed the combined steady suction and blowing around the window and at the mid-height of the base and attained a η of 3.5 and a DR of 13%. Obviously, the combination of S1, S2, S3 and S4 achieves the best performance when taking both DR and η into account, suggesting a promising control scheme for future applications. Its highest DR is 25% with $\eta > 1$.

4. Conclusions

A rather extensive and thorough study has been performed on the active DR of an Ahmed body (φ = 25º), based on steady blowing jets, at $Re = 1.7 \times 10^5$. A detailed investigation is conducted on four types of individual actuations and their combinations deployed around the rear window and the vertical base of the model. Extensive flow measurements are also conducted to understand the mechanisms behind the DR. Following conclusions can be drawn out of this work.

A maximum DR by 12% is achieved by actuation S_1 deployed along the upper edge of the rear window. Under this control, flow separation is postponed from the upper edge of the rear window to downstream of the actuation ($x^* \approx -0.24$ on the slanted surface). The separated shear layer runs into the recirculation flow behind the vertical base, without reattaching on the slanted surface. The upper and lower recirculation bubbles behind the base grow substantially in size, and the alternately emanated organized structures from the two bubbles (Zhang *et al.* 2015) disappear. As a result, the spatially averaged pressure coefficients $\langle C_p \rangle_{\mathrm{CR}}$, $\langle C_p \rangle_{\mathrm{LR}}$ and $\langle C_p \rangle_{\mathrm{CB}}$ are increased by 21%, 17% and 15%, respectively. On the other hand, actuation S_2 along the two side edges of the rear window produces a maximum DR of 6% since the C-pillar vortices are substantially weakened. This rather limited reduction in drag is associated with a pressure rise by 1%, 6% and 3% for $\langle C_p \rangle_{\mathrm{CR}}$, $\langle C_p \rangle_{\mathrm{LR}}$ and $\langle C_p \rangle_{\mathrm{CB}}$, respectively. The combination of S_1 and S_2 is deployed to manipulate simultaneously the separation bubble and the C-pillar vortices over the rear window, achieving a maximum DR by 16%. Meanwhile, $\langle C_p \rangle_{\mathrm{CR}}$, $\langle C_p \rangle_{\mathrm{LR}}$ and $\langle C_p \rangle_{\mathrm{CB}}$ rise by 22%, 19% and 19%, respectively, higher than those produced by S_1 or S_2.

Actuations S_3 and S_4 are applied along the upper and lower edges of the vertical base, respectively, and can either substantially reduce or increase the drag, depending on the blowing angles. Actuations S_3 at $\theta_{S3} = 45°$ and S_4 at $\theta_{S4} = 45°$ lead to maximum reductions in drag by 11% and 14%, respectively. In both cases, flow separation from the rear window is found to be postponed from the upper edge to $x^* \approx -0.5$. In contrast to the case under S_1, the separated shear layer reattaches downstream, forming a separation bubble over the rear window. The flow reattaches at $x^* \approx -0.08$ under S_4, upstream of that ($x^* \approx -0.02$) under S_3. This difference accounts for the higher pressure rise, 16%, in $\langle C_p \rangle_{\mathrm{CR}}$ under S_4 than that (14%) under S_3. Meanwhile, the C-pillar vortices are weakened in strength. As a result, $\langle C_p \rangle_{\mathrm{LR}}$ rises. Behind the vertical base, the upper and lower recirculation bubbles expand longitudinally by 40% and 25%, respectively, under S_3, larger than those (26% and 11%) under S_4. This expansion may have acted to suppress the dynamic process of the bubble expansion and burst, as found by Zhang *et al.* (2015), and the alternate emanation of the coherent structures from the two bubbles disappears. This may imply more stagnant fluid in the recirculation region, thus resulting in the increased pressure on the base. Combining S_3 and S_4 produces a maximum DR of 18%. Flow separation is postponed to $x^* \approx -0.45$ on the rear window, and the separated shear layer reattaches downstream at $x^* \approx -0.05$, forming a separation bubble on the slanted surface. Again, the C-pillar vortices are weakened in strength, and $\langle C_p \rangle_{\mathrm{CR}}$ and $\langle C_p \rangle_{\mathrm{LR}}$ are increased by 23% and 21%, respectively, exceeding those (14% and 12%) under S_3 or those (16% and 14%) under S_4. The upper and lower bubbles behind the base are prolonged by 38% and 23%, respectively, compared to the base flow, with almost the same growth as those (40% and 25%) under S_3 but exceeding those (26% and 11%) under S_4. Consequently, the rise (24%) in $\langle C_p \rangle_{CB}$ under S_3 and S_4 is comparable with that (25%) under S_3, but higher than that (21%) under S_4.

Under the combination of all four actuations, a separation bubble occurs over the rear window due to flow separation at $x^* \approx -0.43$ and reattachment at $x^* \approx -0.06$. Control-generated structures are entrained into the bubble, resulting in a pressure rise on the slanted surface and an increase in $\langle C_p \rangle_{\mathrm{CR}}$ by 40%. The C-pillar vortices are substantially impaired, which is associated with a rise in $\langle C_p \rangle_{\mathrm{LR}}$ by 32%. The upper and lower recirculation bubbles behind the vertical base grow longitudinally by 56% and 43%, respectively. This growth implies an impaired strength in the bubbles and hence the disappearance of the alternately emanated organized structures from the two bubbles. Subsequently, $\langle C_p \rangle_{\mathrm{CB}}$ rises by 30%. The combination of S_1, S_2, S_3 and S_4 produces a maximum DR by 29%.

The combinations of (S_1, S_2 and S_3) and (S_1, S_2 and S_4) may achieve a maximum DR by 25% and 26%, respectively. In both cases, a separation bubble, with its size comparable to that under the combination of S_1, S_2, S_3 and S_4, is generated on the rear window. There appears an entrainment of control-generated structures into the separation bubble from the lower end of the slanted surface under the combined S_1, S_2 and S_3, or from the vertical base under the combined S_1, S_2 and S_4. Accordingly, $\langle C_p \rangle_{\mathrm{CR}}$ rises by 35% for the former and by 36% for the latter, while $\langle C_p \rangle_{\mathrm{LR}}$ increases by 30% for both cases due to the weakened C-pillar vortices. Furthermore, the upper and lower recirculation bubbles behind the base are longitudinally enlarged and the alternate emanation of organized structures from the two bubbles is not observed anymore, accounting for a rise in $\langle C_p \rangle_{\mathrm{CB}}$ by 25% under S_1, S_2 and S_3 and 27% under S_1, S_2 and S_4.

The control efficiency is assessed for each scheme. Individual actuations S_1, S_2, S_3 and S_4 may achieve an η of 37.5, 32.8, 16.1 and 8.4, respectively, at small momentum coefficients. When S_3 or S_4 produces its maximum DR (11% or 14%), the required power input is rather large and the corresponding efficiency is very low. In fact, η is less than unity, 0.21 under S_3 or 0.26 under S_4. The combinations (S_1 and S_2) and (S_3 and S_4) lead to η up to 34.3 and 5.8, corresponding to the DRs of 7% and 2%, respectively. The maximum η achieved is 4.4 with the combination of S_1, S_2, S_3 and S_4 and the corresponding DR is 18%. When the combination of S_1, S_2, S_3 and S_4 produces a DR by 29%, the corresponding control efficiency is very low, $\eta = 0.36$, due to a large energy consumption.

Acknowledgements

YZ wishes to acknowledge support given to him from NSFC through grants 11632006, 91752109 and U1613226, from Research Grants Council of HKSAR through grant GRF 531912 and from Research Grants Council of Shenzhen Government through grants JCYJ20160531193220561 and JCY20160531192108351.

References

AHMED, S. R., RAMM, R. & FALTIN, G. 1984 Some salient features of the time-averaged ground vehicle wake. *SAE Technical paper* 840300, 1-30, Society of Automotive Engineers, Inc., Warrendale, PA.

AUBRUN, S., MCNALLY, J., ALVI, F. & KOURTA, A. 2011 Separation flow control on a generic ground vehicle using steady microjet arrays. *Exp. Fluids* **51**, 1177-1187.

BARROS, D., RUIZ, T., BORÉE, J. & NOACK, B. R. 2014 Control of a three-dimensional blunt body wake using low and high frequency pulsed jets. *Int. J. Flow Contr* **6**, 61-73.

BARROS, D., BORÉE, J. NOACK, B. R. & SPOHN, A. 2016 Bluff body drag manipulation using pulsed jets and Coanda effect. *J. Fluid Mech.* **805**, 422-459.

BELLMAN, M., AGARWAL, R., NABER, J. & CHUSAK, L. 2010 Reducing energy consumption of ground vehicles by active flow control. ASME Paper No. ES2010-90363.

BEAUDOIN, J. F. & AIDER, J. L. 2008 Drag and lift reduction of a 3D bluff body using flaps. *Exps. Fluids* **44**, 491-501.

BIDEAUX, E., BOBILLIER, P., FOURNIER, E., GILLIÉRON, P., HAJEM, M. E., CHAMPAGNE, J. Y., GILOTTE, P. & KOURTA, A. 2011 Drag reduction by pulsed jets on strongly unstructured wake: towards the square back control. *Int. J. Aerodynamics* **1**, 282-298.

BIDKAR, R. A., LEBLANC, L., KULKARNI, A. J., BAHADUR, V., CECCIO, S. L. & PERLIN, M. 2014 Skin-friction drag reduction in the turbulent regime using random-textured hydrophobic surfaces. *Phys. Fluids* **26**, 085108

BOUCINHA, V., WEBER, R. & KOURTA, A. 2011 Drag reduction of a 3D bluff body using plasma actuators. *Int. J. Aerodynamics* **1**, 262-280.

BRUNEAU, C., CREUSE, E., DELPHINE, D., GILLIÉRON, P. & MORTAZAVI, I. 2011 Active procedures to control the flow past the Ahmed body with a 25° rear window. *Int. J. Aerodynamics* **1**, 299-317.

BRUNN, A., WASSEN, E., SPERBER, D., NITSCHE, W. & THIELE, F. 2007 Active drag control for a generic car model, *Active Flow Control, NNFM,* **95**, 247-259.

BRUNN, A., NITSCHE, W., HENNING, L. & KING, R. 2008 Application of slope-seeking to a generic car model for active drag control. AIAA Paper No. 2008-6734.

CATTAFESTA, L. N. & SHEPLAK, M. 2011 Actuators for active flow control. *Annu. Rev. Fluid Mech.* **43**, 247-272.

CENGEL, Y. A. & CIMBALA, J. M. 2010 Fluid Mechanics: Fundamentals and Applications, 2nd ed. McGrow Hill Inc., New York, pp 580-590. ISBN: 0077295463.

CHOI, H., JEON, W. P. & KIM, J. 2008 Control of flow over a bluff body. *Annu. Rev. Fluid Mech.* **40**, 113-139.

CHOI, H., LEE, J. & PARK, H. 2014 Aerodynamics of heavy vehicles. *Annu. Rev. Fluid Mech.* **46**, 441-468.

CORKE, T. C., ENLOE, C. L. & WILKINSON, S. P. 2010 Dielectric barrier discharge plasma actuators for flow control. *Annu. Rev. Fluid Mech.* **42**, 505-529.

EVSTAFYEVA, O., MORGANS, A. S. & DALLA LONGA, L. 2017 Simulation and feedback control of the Ahmed body flow exhibiting symmetry breaking behavior. *J. Fluid Mech.* **817**, R2

GAD-EL-HAK, M. 2000 *Flow Control: Passive, Active, and Reactive Flow Management*. Cambridge University Press.

GILLIÉRON, P. & KOURTA, A. 2013 Aerodynamic drag control by pulsed jets on simplified car geometry. *Exp. Fluids* **54**, 1457, 1-16.

GLEZER, A. & AMITAY, M. 2002 Synthetic jets. *Annu. Rev. Fluid Mech.* **34**, 503-529

GOMES-FERNANDES, R., GANAPATHISUBRAMANI, B. & VASSILICOS, J. C. 2012 Particle image velocimetry study of fractal-generated turbulence. *J. Fluid Mech.* **711**, 306-336.

GRANDEMANGE, M., GOHLKE, M. & CADOT, O. 2013 Turbulent wake past a three-dimensional blunt body. Part 1. Global modes and bi-stability. *J. Fluid Mech.* **722**, 51-84..

HOWARD, R. J. A. & POURQUIE, M. 2002 Large eddy simulation of an Ahmed reference model. *Journal of Turbulence* **3**, 012

HUCHO, W. H. & SOVRAN, G. 1993 Aerodynamics of road vehicles. *Ann. Rev. Fluid Mech.* **25**, 485-537.

HUANG, J. F., ZHOU, Y. & ZHOU, T. M. 2006 Three-dimensional wake structure measurement using a modified PIV technique. *Exp. Fluids* **40**, 884-896.

JOHNSTON, J. P. & NISHI, M. 1990 Vortex generator jets – means for flow separation control. *AIAA Journal*, 28, 989-994.

JOSEPH, P., AMANDOLESE, X. & AIDER, J. L. 2012 Drag reduction on the 25° slant angle Ahmed reference body using pulsed jets. *Exps. Fluids* **52**, 1169-1185.

JOSEPH, P., AMANDOLESE X., EDOUARD, C. & AIDER, J. L. 2013 Flow control using MEMS pulsed micro-jets on the Ahmed body. *Exp. Fluids* **54**, 1442, 1-12 pages.

KIM, J., HAHN, S., KIM, J., LEE, D. K., CHOI, J., JEON, W. P. & CHOI, H. 2004 Active control of turbulent flow over a model vehicle for drag reduction. *J. Turbulence* **5**, 1-12.

KOURTA, A. & LECLERC, C. 2013 Characterization of synthetic jet actuation with application to Ahmed body wake. *Sensors and Actuators A* **192**, 13-26.

KRENTEL, D., MUMINOVIC, R., BRUNN, A., NITSCHE, W. & KING, R. 2010 Application of active flow control on generic 3D car models. *Active Flow Control. NNFM* **108**, 223-239.

KUMAR, V. & ALVI, F. 2006 Use of high-speed microjets for active separation control in diffusers. *AIAA Journal*, **44**, 273-281.

LIENHART, H. & BECKER, S. 2003 Flow and turbulent structures in the wake of a simplified car model. *SAE Technical paper* 2003-01-0656, Society of Automotive Engineers, Inc., Warrendale, PA.

LITTLEWOOD, R. & PASSMORE, M. 2012 Aerodynamic drag reduction of a simplified squareback vehicle using steady blowing. *Exp. Fluids* **53**, 519-529.

LUCAS, J. M., CADOT, O., HERBERT, V., PARPAIS, S. & DÉLERY, J. 2017 A numerical investigation of the asymmetric wake mode of a squareback Ahmed body – effect of base cavity. *J. Fluid Mech.* **831**, 675-697.

MCNALLY, J., FERNANDEZ, E., ROBERTSON, G., KUMAR, R., TAIRA, K., ALVI, F., YAMAGUCHI, Y. & MURAYAMA, K. 2015 Drag reduction on a flat-back ground vehicle with active flow control. *J. Wind Eng Ind Aerodyn* **145**: 292-303

METKA, M. & GREGORY, J. W. 2015 Drag reduction on the 25-deg Ahmed model using fluidic oscillators. *J. Fluids Eng.* **137**, 051108.

NABAVI, M., SIDDIQUI, M. H. K. & DARGAHI, J. 2008 Experimental investigation of the formation of acoustic streaming in a rectangular enclosure using a synchronized PIV technique. *Meas. Sci. Technol.* **19**, 065405

PARK, H., CHO, J. H., LEE, J., LEE, D. H. & KIM, K. H. 2013 Experimental study on synthetic jet array for aerodynamic drag reduction of a simplified car model. *J. Mech. Sci. and Technol.* **27**, 3721-3731.

PASTOOR, M., HENNING, L., NOACK, B., KING, R. & TADMOR, G. 2008 Feedback shear layer control for bluff body drag reduction. *J. Fluid Mech.* **608**,161-196.

PERNOD, P., MERLEN, A., TALBI, A., PREOBRAZHENSKY, V., VIARD, R., GIMENO, L. & DUCLOUX, O. 2011 IEMN/LEMAC magneto-mechanical microjets and micro-hotwires and aerodynamic active flow control. *Int. J. Aerodynamics* **1**, 243-261.

PUJALS, G., DEPARDON, S. & COSSU, C. 2010 Drag reduction of a 3d bluff body using coherent streamwise streaks. *Exp. Fluids* **49**, 1085-1094.

QUINN, D. B., LAUDER, G. V. & SMITS, A. J. 2014 Scaling the propulsive performance of heaving flexible panels.

J. Fluid Mech. **738**, 250-267.

RAFFEL, M., WILLERT, C. E., WERELY, S. T. & KOMPENHANS, J. 2007 Particle Image Velocimetry: A Practical Guide. 2nd ed. Springer

RAJAMANICKAM, K. & BASU, S. 2017 On the dynamics of vortex-droplet interactions, dispersion and breakup in a coaxial swirling flow. *J. Fluid Mech.* **827**, 572-613.

ROSSITTO, G., SICOT, C., FERRAND, V., BORÉE, J. & HARAMBAT, F. 2016 Influence of afterbody rounding on the pressure distribution over a fastback vehicle. *Exp. Fluids* **57**, 43, 1-12.

ROUMÉAS, M., GILLIÉRON, P. & KOURTA, A. 2009a Analysis and control of the near-wake flow over a square-back geometry. *Computers & Fluids* **38**, 60-70.

ROUMÉAS, M., GILLIÉRON, P. & KOURTA, A. 2009b Drag Reduction by Flow Separation Control on a Car After Body. *Int. J. Numer. Methods Fluids* **60**, 1222-1240.

SCIACCHITANO, A., WIENEKE, B. & SCARANO, F. 2013 PIV uncertainty quantification by image matching. *Meas. Sci. Technol.* **24**, 045302.

SEIFERT, A., STALNOV, O., SPERBER, D., ARWATZ, G., PALEI, V., DAVID, S., DAYAN, I. & FONO, I. 2008 Large trucks drag reduction using active flow control. AIAA Aerosp. Sci. Meet. Exh., Reno, Nev., Paper No. 2008-743.

SUDIN, M. N., ABDULLAH, M. A., SHAMSUDDIN, S. A., RAMLI, F. R. & TAHIR, M. M. 2014 Review of research on vehicles aerodynamic drag reduction methods. *Int. J. Mech. Mechatron Eng.* **14**, 35-47.

THACKER, A., AUBRUN, S., LEROY, A. & DEVINANT, P. 2012 Effects of suppressing the 3D separation on the rear slant on the flow structures around an Ahmed body. *J. Wind Eng. Ind. Aerodyn.* **107-108**, 237-243.

TOUNSI, N., MESTIRI, R., KEIRSBULCK, L, OUALLI, H., HANCHI, S. & ALOUI, F. 2016 Experimental study of flow control on bluff body using piezoelectric actuators. *J. Appl. Fluid Mech.* **9**, 827-838.

VENNING, J., JACONO, D. L., BURTON, D., THOMPSON, M. C. & SHERIDAN, J. 2017 The nature of the vortical structures in the near wake of the Ahmed body. *Proc IMechE Part D: J. Automobile Engineering*, 1-6.

VERZICCO, R., FATICA, M., IACCARINO, G. & MOIN, P. 2002 Large eddy simulation of a road vehicle with drag-reduction devices. *AIAA Journal* **40**, 2447-55.

WANG, X. W., ZHOU, Y., PIN, Y. F. & CHAN, T. L. 2013 Turbulent near wake of an Ahmed vehicle model. *Exp. Fluids* **54**, 1490, 1-19.

WASSEN, E. & THIELE, F. 2008 Drag Reduction for a Generic Car Model Using Steady Blowing. AIAA Paper No. 2008-3771.

WASSEN, E. & THIELE, F. 2009 Road vehicle drag reduction by combined steady blowing and suction. AIAA Paper No. 2009-4174.

WASSEN, E. & THIELE, F. 2010 Simulation of Active Separation Control on a Generic Vehicle. AIAA Paper No. 2010-4702.

WEN, X., TANG, H. & DUAN, F. 2015 Vortex dynamics of in-line twin synthetic jets in a laminar boundary layer. *Phys. Fluids* **27**, 083601

YANG, H. & ZHOU, Y. 2016 Axisymmetric jet manipulated using two unsteady minijets, *J. Fluid Mech.* **808,** 362-396.

ZHANG, B. F., ZHOU, Y. & TO, S. 2015 Unsteady flow structures around a high-drag Ahmed body. *J. Fluid Mech.* **777**, 291-326.

ZHOU, Y., DU, C., MI, J. & WANG, X. W. 2012 Turbulent round jet control using two steady mini-jets. *AIAA Journal* **50**, 736-740.

Tables and figures

Researchers	Actuation technique	Actuation location	BR^{j}	C_μ^{j}	$f^{\mathrm{j}*}$	Jet configuration	$Re/10^5$	Maximum DR
Brunn *et al.* (2007)	Steady blowing	Two upper corners of rear window	0.19 ~ 0.84	$(0.9 \sim 17.9)\times10^{-3}$	–	3D	1.6	3%
Brunn *et al.* (2008)	Combination of steady blowing S_{a1} and pulsed blowing P_{a2} and P_{a3}	S_{a1}: two upper corners of rear window; P_{a2} and P_{a3}: upper and lower edges of base, respectively	$BR^{\mathrm{Sa1}}=$ 0.37 ~ 0.65; $BR^{\mathrm{Pa2}}=1.2$; $BR^{\mathrm{Pa2}}=1.2$	$C_\mu^{\mathrm{Sa1}}=(3.6 \sim 10.8)\times10^{-3}$; $C_\mu^{\mathrm{Pa2}}=17.9\times10^{-3}$; $C_\mu^{\mathrm{Pa3}}=17.9\times10^{-3}$	$f^{\mathrm{pa2}*}=f^{\mathrm{pa3}*}$ = 0.03 ~ 0.58	S_{a1}: 3D; P_{a2} and P_{a3}: 2D	1.3	13%
Wassen & Thiele (2008)	Combination of steady blowing S_{b1}, S_{b2}, S_{b3} and S_{b4}	S_{b1} and S_{b2}: upper and two side edges of rear window, respectively; S_{b3} and S_{b4}: lower and two side edges of base, respectively	$BR^{\mathrm{Sb1}}=1$; $BR^{\mathrm{Sb2}}=1$; $BR^{\mathrm{Sb3}}=1$; $BR^{\mathrm{Sb4}}=1$	$C_\mu^{\mathrm{Sb1}}=6.1\times10^{-3}$; $C_\mu^{\mathrm{Sb2}}=6.9\times10^{-3}$; $C_\mu^{\mathrm{Sb3}}=14.5\times10^{-3}$; $C_\mu^{\mathrm{Sb4}}=14.3\times10^{-3}$	–	2D for each actuation	1.6	6%
Wassen & Thiele (2009)	Alternate steady blowing and suction	Upper edge of rear window	1	4.8×10^{-3}	–	3D	1.6	9%
Wassen & Thiele (2010)	Combination of steady blowing S_{c1}, S_{c2}, S_{c3} and S_{c4}	S_{c1} and S_{c2}: upper and two side edges of rear window, respectively; S_{c3} and S_{c4}: lower and two side edges of base, respectively	$BR^{\mathrm{Sc1}}=1$; $BR^{\mathrm{Sc2}}=1$; $BR^{\mathrm{Sc3}}=1$; $BR^{\mathrm{Sc4}}=1$	$C_\mu^{\mathrm{Sc1}}=12.9\times10^{-3}$; $C_\mu^{\mathrm{Sc2}}=14.9\times10^{-3}$; $C_\mu^{\mathrm{Sc3}}=10.2\times10^{-3}$; $C_\mu^{\mathrm{Sc4}}=10.1\times10^{-3}$	–	2D for each actuation	1.6	10%
Krentel *et al.* (2010)	Pulsed blowing	Upper edge of base	1.5	7.2×10^{-3}	0 ~ 0.69	3D	3.2	6%
Aubrun *et al.* (2011)	Steady blowing	Upper edge of rear window	0.63 ~ 5.2	$(0.1 \sim 6.6)\times10^{-3}$	–	3D	3.1 ~ 6.2	14%
Bruneau *et al.* (2011)	Combination of steady suction S_{d1} and blowing S_{d2} and S_{d3}	S_{d1} and S_{d2}: upper and two side edges of rear window, respectively; S_{d3}: mid-height of base	$BR^{\mathrm{Sd1}}=0.6$; $BR^{\mathrm{Sd2}}=0.6$; $BR^{\mathrm{Sd3}}=0.6$	$C_\mu^{\mathrm{Sd1}}=14.5\times10^{-3}$; $C_\mu^{\mathrm{Sd2}}=18.3\times10^{-3}$; $C_\mu^{\mathrm{Sd3}}=16.1\times10^{-3}$	–	2D for each actuation	0.1	13%
Pernord *et al.* (2011)	Pulsed blowing	Upper edge of rear window	1 ~ 11	$(0.5 \sim 65.7)\times10^{-3}$	0 ~ 1.2	3D	1.5 ~ 6.1	6%
Boucinha *et al.* (2011)	Plasma actuator	Upper edge of rear window	–	–	0.03~1.8	2D	2.3	8%
Joseph *et al.* (2012)	Pulsed blowing	Near the end of roof	0.31 ~ 1.1	$(0.3 \sim 3.6)\times10^{-3}$	0 ~ 1.6	3D	4.5	8%
Joseph *et al.* (2013)	Pulsed blowing	Near the end of roof	1.1 ~ 4.1	$(0.5 \sim 7.5)\times10^{-3}$	0.7 ~ 2.9	3D	3.5 ~ 6.7	10%
Park *et al.* (2013)	Synthetic jet	Upper edge of rear window	0.16 ~ 1.1	$(0.2 \sim 10.9)\times10^{-3}$	0.47 ~ 2.1	3D	1.4	5%
Kourta & Leclerc (2013)	Synthetic jet	Near the end of roof	0.05 ~ 0.44	$(0.01 \sim 0.7)\times10^{-3}$	0.29 ~ 6.6	3D	3.9 ~ 6.1	9%
Metka & Gregory (2015)	Fluidic oscillator	Upper edge of rear window	1.5 ~ 5.8	$(2.5 \sim 37.2)\times10^{-3}$	7.5 ~ 29.9	3D	4.5	7%
Tounsi *et al.* (2016)	Synthetic jet	Upper edge of rear window	0.09 ~ 0.37	$(0.05 \sim 0.9)\times10^{-3}$	2.4 ~ 8.9	3D	3.2 ~ 9.6	10%

TABLE 1. Summary of studies on active DR of an Ahmed body ($\varphi = 25°$). The blowing ratio BR^{j} and momentum coefficient C_μ^{j} are calculated based on the mean exit (or inlet) velocity for steady blowing (or suction), pulsed blowing and fluidic oscillators. Superscript 'j' denotes individual actuations. For synthetic jets, the BR^{j} and C_μ^{j} are estimated by the mean exit velocity during the outstroke. The Reynolds number Re and the normalized actuation frequency $f^{\mathrm{j}*}$ are calculated based on the square root of model frontal area and free-stream velocity.

Cases	C_μ^{Si}	BR^{Si}	$\Delta\langle C_p\rangle_{\mathrm{CR}}$	$\Delta\langle C_p\rangle_{\mathrm{LR}}$	$\Delta\langle C_p\rangle_{\mathrm{CB}}$	$\Delta\langle C_p\rangle_{\mathrm{LB}}$	$\Delta\langle C_p\rangle$	ΔC_D
Actuation S_1	C_μ^{S1}=1.1 × 10^{-2}	BR^{S1} = 2.0	21%	17%	15%	-12%	12%	-12%
Actuation S_2	C_μ^{S2}=0.7 × 10^{-2}	BR^{S2} = 0.8	1%	6%	3%	-2%	3%	-6%
Actuation S_3	C_μ^{S3}=6.9 × 10^{-2}	BR^{S3} = 5.6	14%	12%	25%	-17%	10%	-11%
Actuation S_4	C_μ^{S4}=6.9 × 10^{-2}	BR^{S4} = 5.6	16%	14%	21%	-15%	11%	-14%
Combined S_1 and S_2	C_μ^{S1}=0.3 × 10^{-2} C_μ^{S2}=2.0 × 10^{-2}	BR^{S1} = 1.1 BR^{S2} = 1.4	22%	19%	19%	-6%	15%	-16%
Combined S_3 and S_4	C_μ^{S3}=8.2 × 10^{-2} C_μ^{S4}=6.9 × 10^{-2}	BR^{S3} = 6.1 BR^{S4} = 5.6	23%	21%	24%	-9%	17%	-18%
Combined S_1, S_2 and S_3	C_μ^{S1}=0.3 × 10^{-2} C_μ^{S2}=2.0 × 10^{-2} C_μ^{S3}=5.6 × 10^{-2}	BR^{S1} = 1.1 BR^{S2} = 1.4 BR^{S3} = 5.1	35%	29%	25%	-11%	23%	-25%
Combined S_1, S_2 and S_4	C_μ^{S1}=0.3 × 10^{-2} C_μ^{S2}=2.0 × 10^{-2} C_μ^{S4}=8.2 × 10^{-2}	BR^{S1} = 1.1 BR^{S2} = 1.4 BR^{S4} = 6.1	36%	31%	27%	-14%	23%	-26%
Combined S_1, S_2, S_3 and S_4	C_μ^{S1}=0.3 × 10^{-2} C_μ^{S2}=2.0 × 10^{-2} C_μ^{S3}=1.9 × 10^{-2} C_μ^{S4}=8.2 × 10^{-2}	BR^{S1} = 1.1 BR^{S2} = 1.4 BR^{S3} = 3.0 BR^{S4} = 6.1	40%	32%	30%	2%	28%	-29%

TABLE 2. DR and pressure recovery achieved under individual S_1 (θ_{S1} = 65°), S_2 (θ_{S2} = 90°), S_3 (θ_{S3} = 45°) and S_4 (θ_{S4} = 45°) and their combinations (Re = 1.7 × 10^5). $\langle C_p\rangle_{\mathrm{CR}}$ and $\langle C_p\rangle_{\mathrm{LR}}$ are spatially averaged pressure coefficients from $C_{p2} \sim C_{p5}$ measured at the centerline (y^* = 0) and $C_{p11} \sim C_{p14}$ near the side edge (y^* = 0.45) of the rear window, respectively, and $\langle C_p\rangle_{\mathrm{CB}}$ and $\langle C_p\rangle_{\mathrm{LB}}$ are the coefficients based on $C_{p6} \sim C_{p10}$ at the centerline (y^* = 0) and $C_{p15} \sim C_{p19}$ near the side edge (y^* = 0.45) of the vertical base, respectively.

Cases	C_μ^{Si}	BR^{Si}	DR	η
Combined S_1 and S_2	$C_\mu^{\mathrm{S1}} = 0.2 \times 10^{-2}$; $C_\mu^{\mathrm{S2}} = 0.1 \times 10^{-2}$	$BR^{\mathrm{S1}} = 0.8$; $BR^{\mathrm{S2}} = 0.3$	7%	34.3
Combined S_1 and S_2	$C_\mu^{\mathrm{S1}} = 0.3 \times 10^{-2}$; $C_\mu^{\mathrm{S2}} = 2.0 \times 10^{-2}$	$BR^{\mathrm{S1}} = 1.1$; $BR^{\mathrm{S2}} = 1.4$	16%	3.9
Combined S_3 and S_4	$C_\mu^{\mathrm{S3}} = 8.2 \times 10^{-2}$; $C_\mu^{\mathrm{S4}} = 6.9 \times 10^{-2}$	$BR^{\mathrm{S3}} = 6.1$; $BR^{\mathrm{S4}} = 5.6$	18%	0.15
Combined S_1, S_2, S_3 and S_4	$C_\mu^{\mathrm{S1}} = 0.3 \times 10^{-2}$; $C_\mu^{\mathrm{S2}} = 2.0 \times 10^{-2}$; $C_\mu^{\mathrm{S3}} = C_\mu^{\mathrm{S4}} = 0.1 \times 10^{-2}$	$BR^{\mathrm{S1}} = 1.1$; $BR^{\mathrm{S2}} = 1.4$; $BR^{\mathrm{S3}} = BR^{\mathrm{S4}} = 0.8$	18%	4.4
Combined S_1, S_2, S_3 and S_4	$C_\mu^{\mathrm{S1}} = 0.3 \times 10^{-2}$; $C_\mu^{\mathrm{S2}} = 2.0 \times 10^{-2}$; $C_\mu^{\mathrm{S3}} = 1.9 \times 10^{-2}$; $C_\mu^{\mathrm{S4}} = 1.9 \times 10^{-2}$	$BR^{\mathrm{S1}} = 1.1$; $BR^{\mathrm{S2}} = 1.4$; $BR^{\mathrm{S3}} = 3.0$; $BR^{\mathrm{S4}} = 3.0$	25%	1.3

TABLE 3. Control efficiency for different combinations of S_1 ($\theta_{S1} = 65°$), S_2 ($\theta_{S2} = 90°$), S_3 ($\theta_{S3} = 45°$) and S_4 ($\theta_{S4} = 45°$) for $Re = 1.7 \times 10^5$.

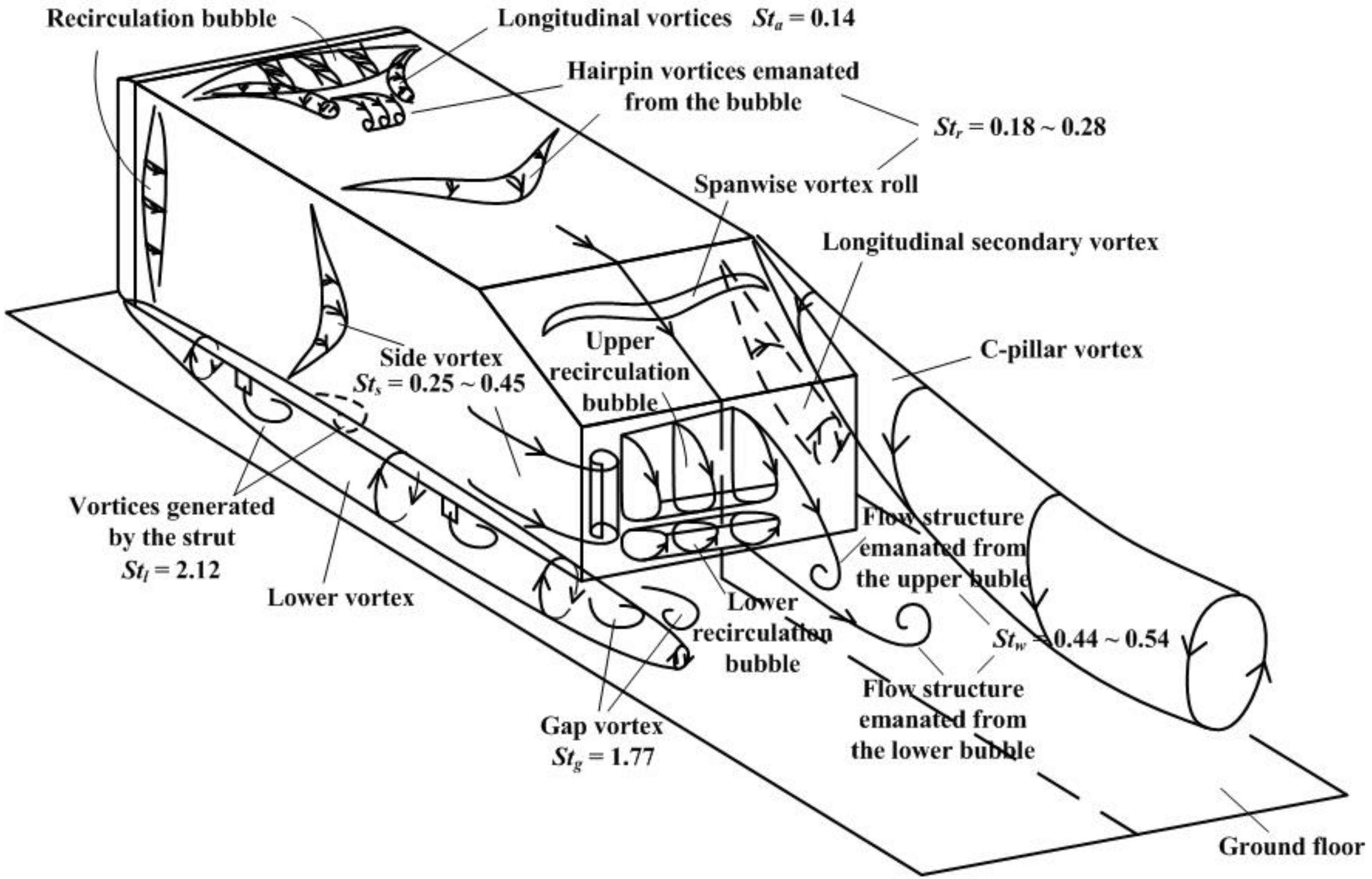

FIGURE 1. A conceptual model of the flow structure around the Ahmed model. The figure is reproduced from Zhang *et al*. (2015).

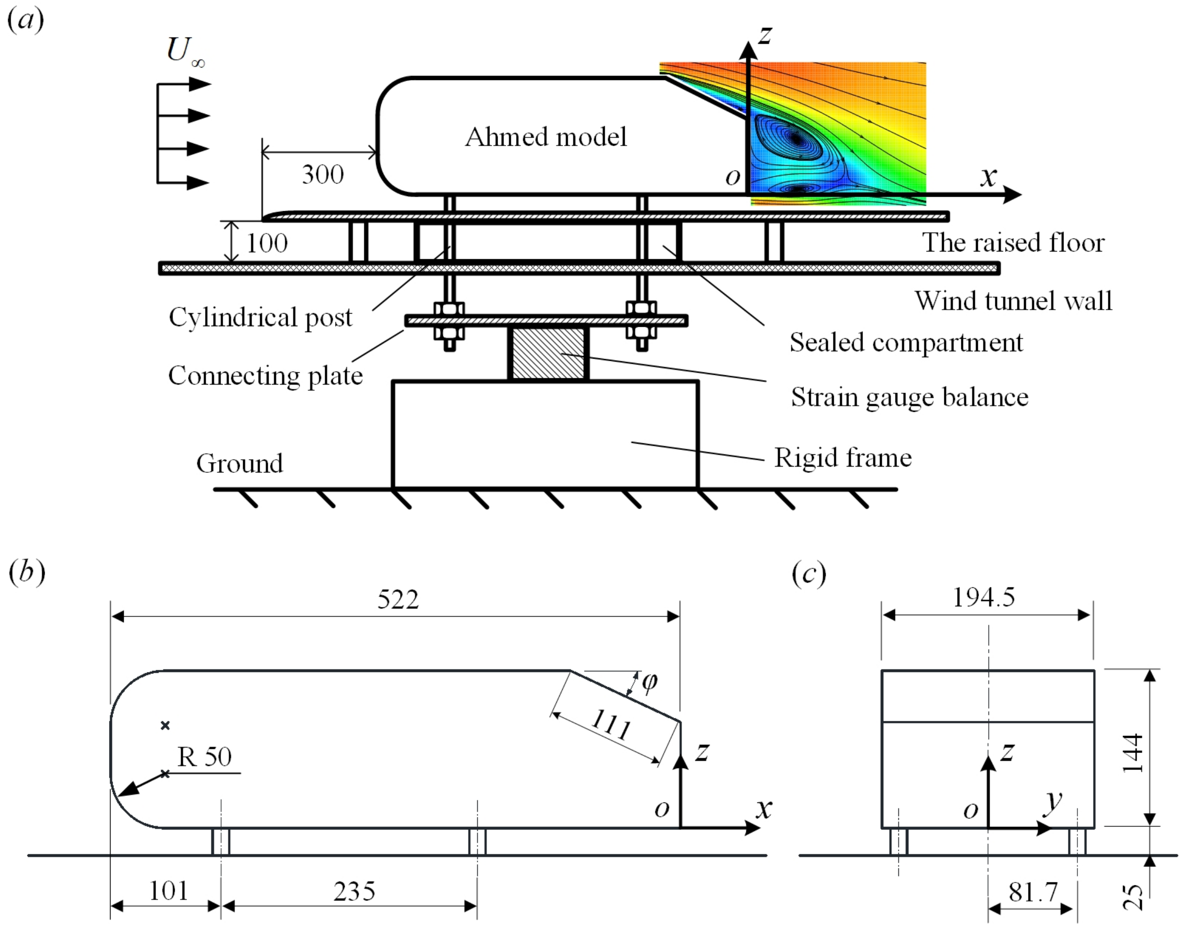

FIGURE 2. (*a*) Schematic of drag measurement setup. Dimensions of a ½-scaled Ahmed body: (*b*) side view, and (*c*) back view. The length unit is mm.

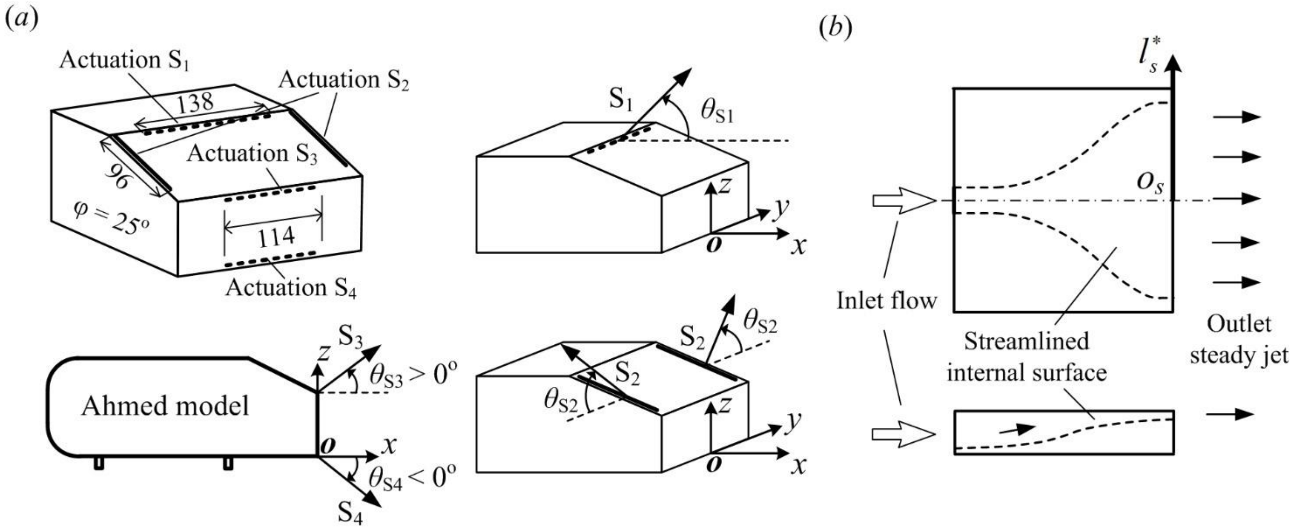

FIGURE 3. (*a*) Arrangement of actuations on the rear slanted surface and the vertical base of the Ahmed model, along with the definitions of the blowing angles, where θ_{S3} and θ_{S4} are positive and negative, respectively. (*b*) Top and side views of the chamber. The length unit is mm.

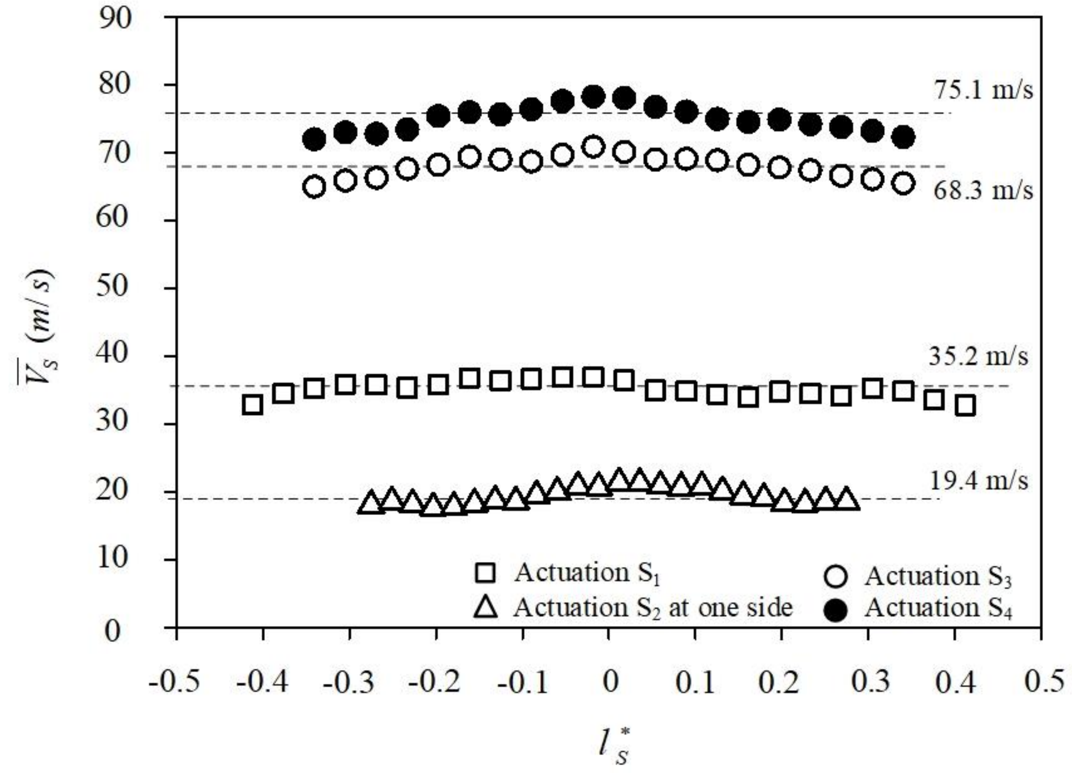

FIGURE 4. Pitot-static-tube-measured time-averaged velocity distribution $\overline{V}_s$ along the slot jet (S_2) or micro-jet arrays (S_1, S_3 and S_4) at 1 mm above the center of jet exit at C_μ^{S1} = 1.3 × 10^{-2} for S_1 (θ_{S1} = 65°), C_μ^{S2}= 2.0 × 10^{-2} for S_2 (θ_{S2} = 90°), C_μ^{S3} = 4.9 × 10^{-2} for S_3 (θ_{S3} = 0°) and C_μ^{S4} = 6.0 × 10^{-2} for S_4 (θ_{S4} = 0°).

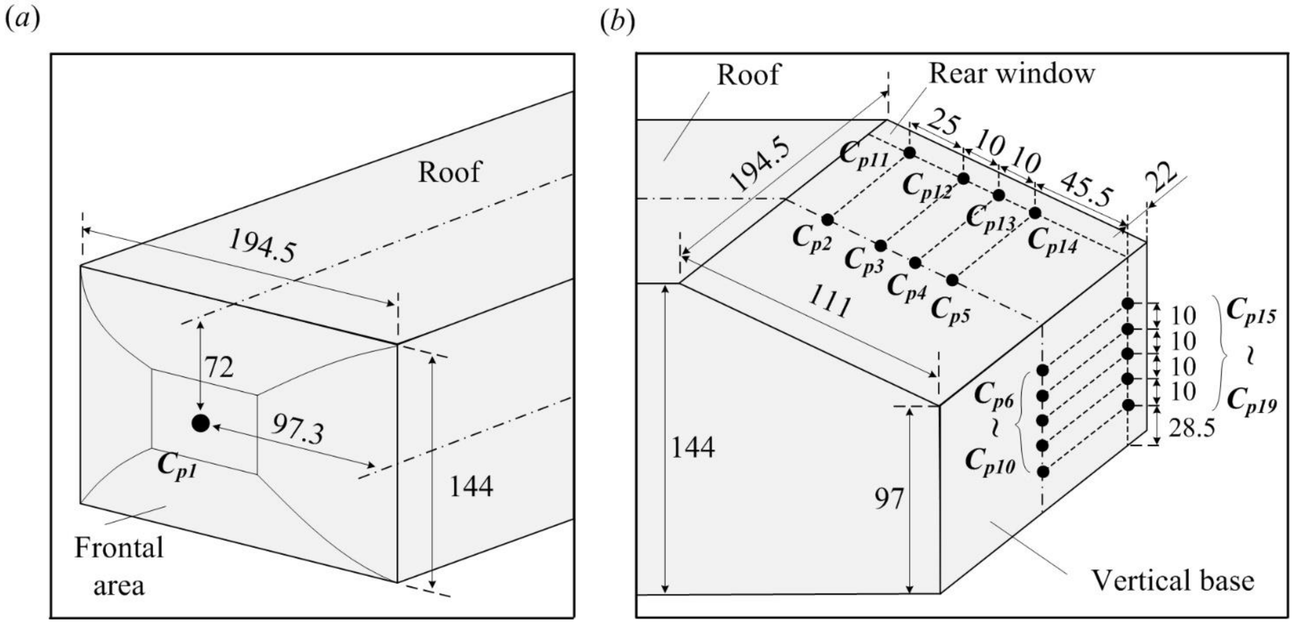

FIGURE 5. Surface pressure measurement locations (*a*) on the frontal face and (*b*) on the rear window and the vertical base of the Ahmed body. The length unit is mm.

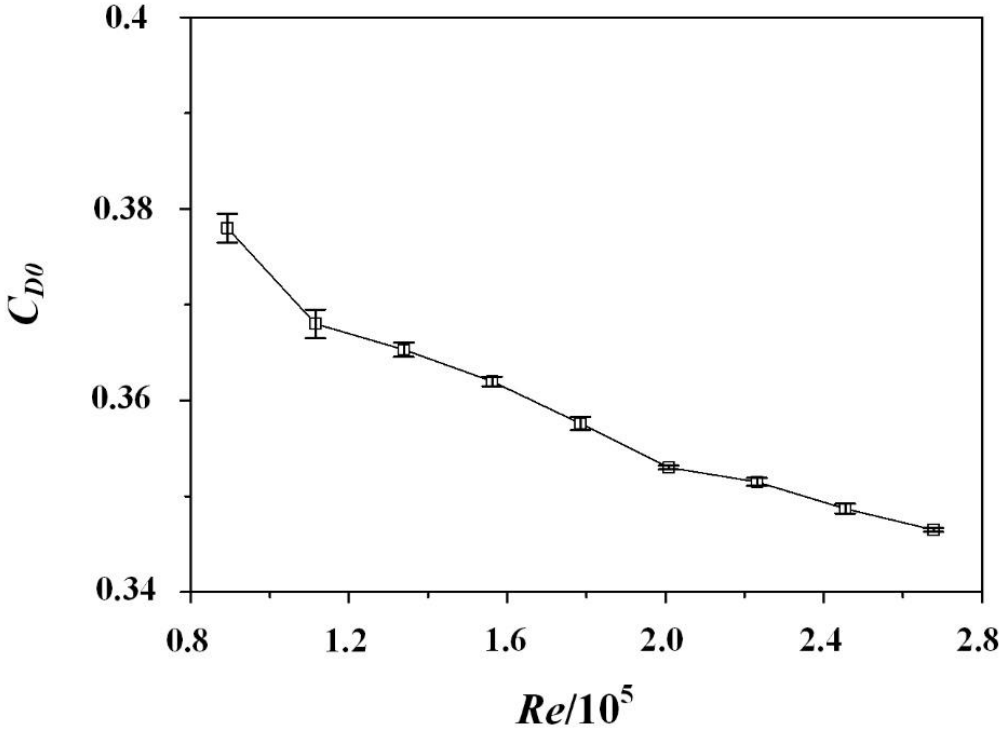

FIGURE 6. Dependence of C_{D0} on Re in the absence of control. The uncertainty bars are given by $\overline{\overline{\left|C_D - \overline{\overline{C_D}}\right|}}$, where the double overbar indicates averaging over three test runs (Bidkar *et al*. 2014).

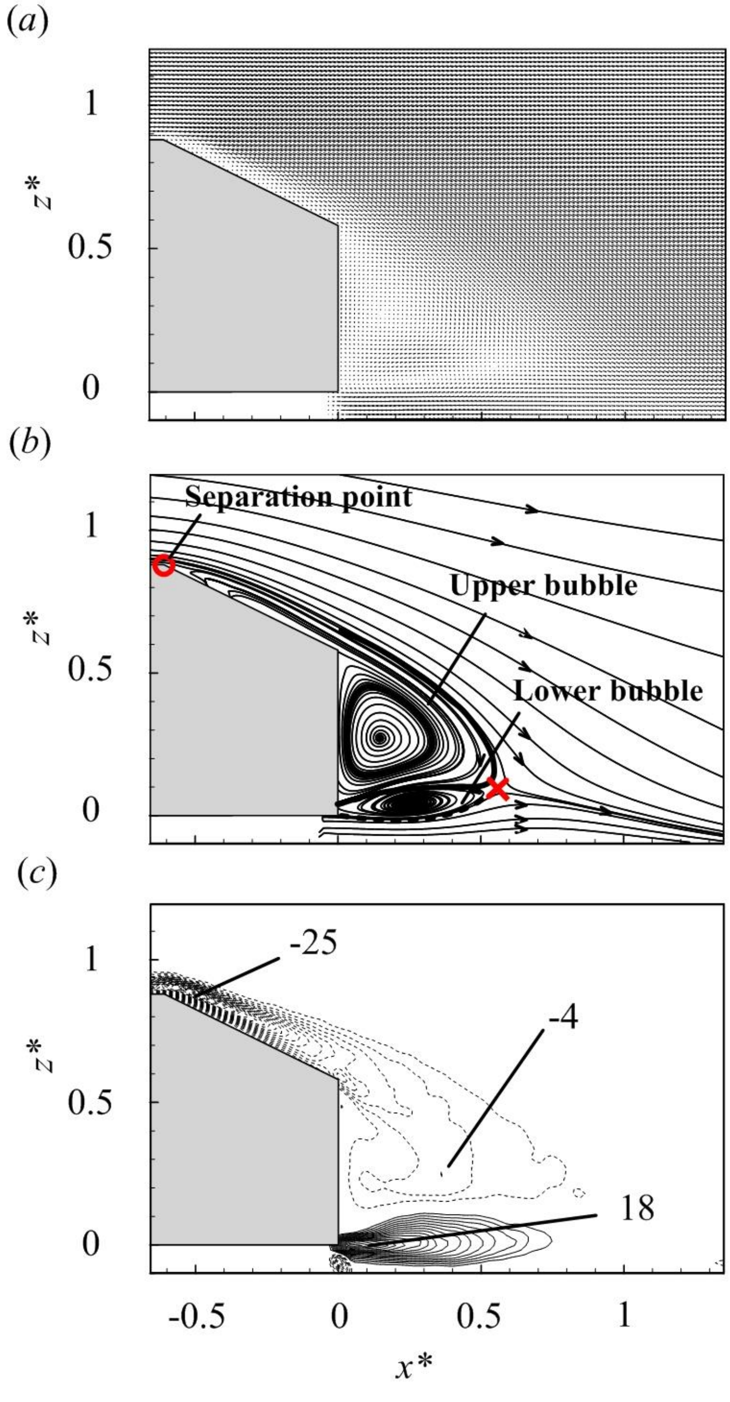

FIGURE 7. (*a*) Time-averaged velocity vectors ($\overline{U}$, $\overline{W}$) measured in the (*x*, *z*) plane of $y^* = 0$, (*b*) corresponding sectional streamlines where red-colored symbol '×' denotes the saddle point, and (*c*) $\overline{\omega_y^*}$-contours where contour interval = 1, the cutoff level = ±2. $Re = 1.7 \times 10^5$.

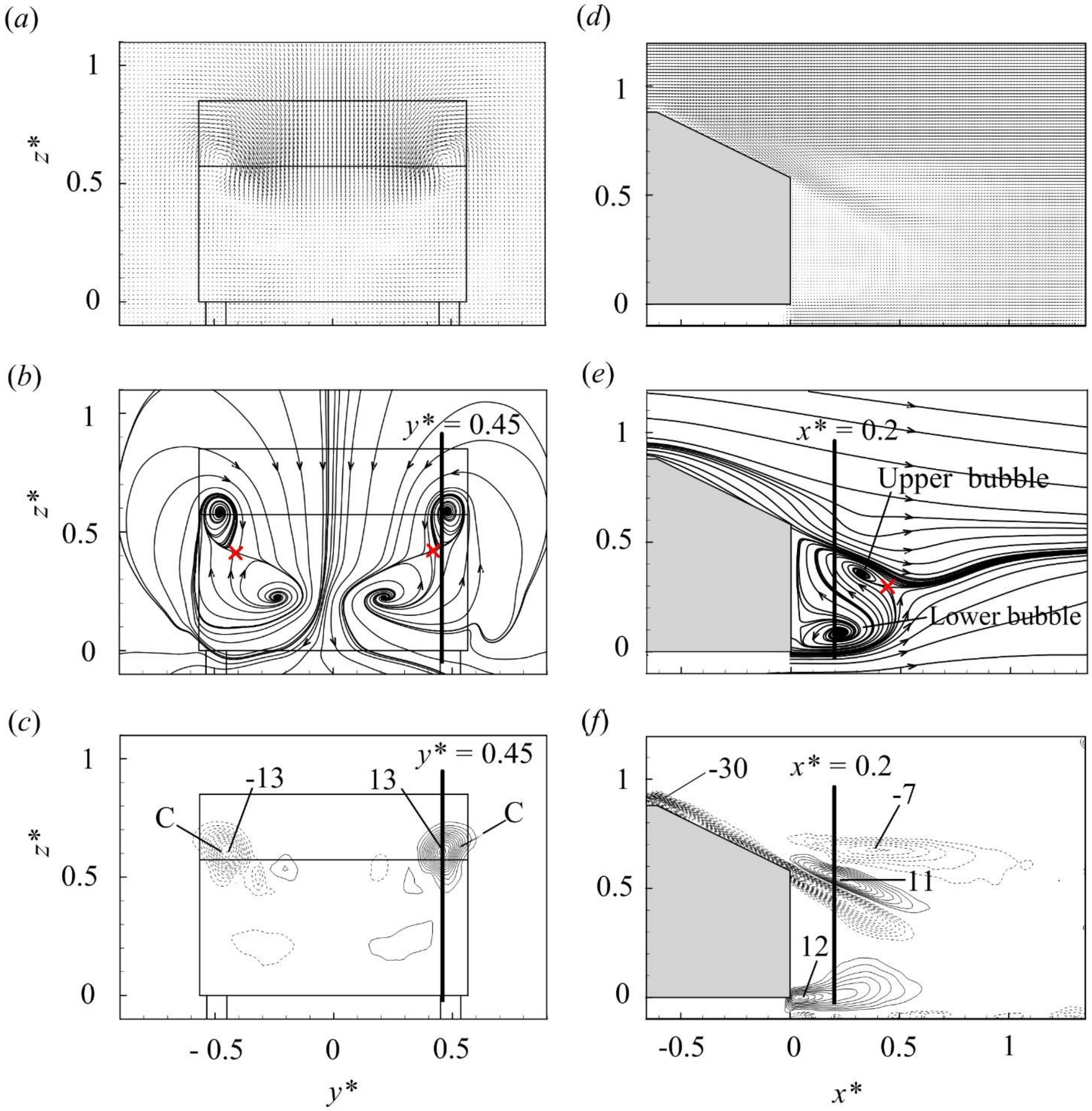

FIGURE 8. (*a*) Time-averaged velocity vectors $(\overline{V}, \overline{W})$, (*b*) streamlines, and (*c*) $\overline{\omega_x^*}$-contours measured in the (*y*, *z*) plane of $x^* = 0.2$. (*d*) Time-averaged velocity vectors $(\overline{U}, \overline{W})$, (*e*) streamlines, and (*f*) $\overline{\omega_y^*}$-contours measured in the (*x*, *z*) plane of $y^* = 0.45$. The vorticity contour interval is 1 and the cutoff level is ±1 for the (*y*, *z*) plane (*c*) and ±2 for the (*x*, *z*) plane (*f*). $Re = 1.7 \times 10^5$.

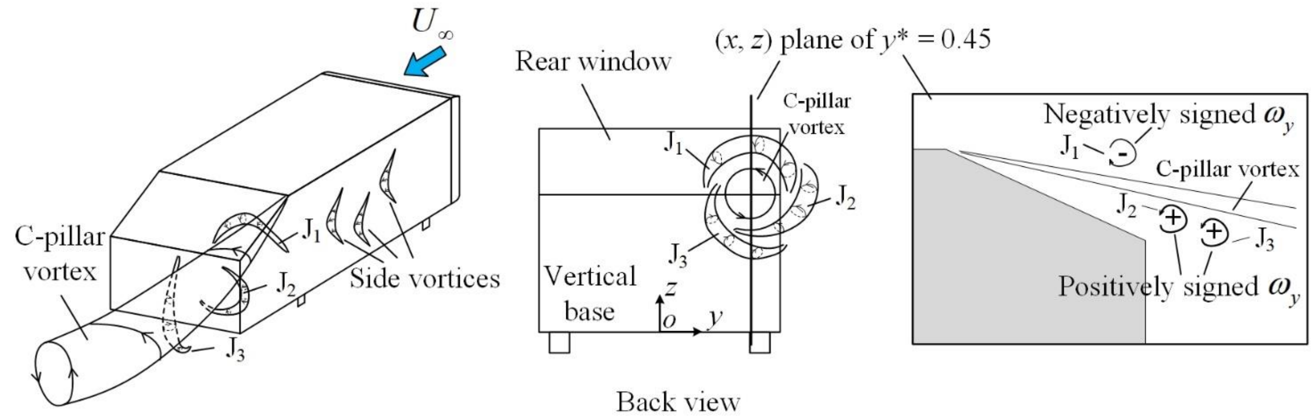

FIGURE 9. Schematic of the formation of unsteady structures near the side edge of the rear window, which are responsible for the oppositely signed $\overline{\omega_y^*}$ concentrations near the upper corner of the vertical base (figure 8*f*).

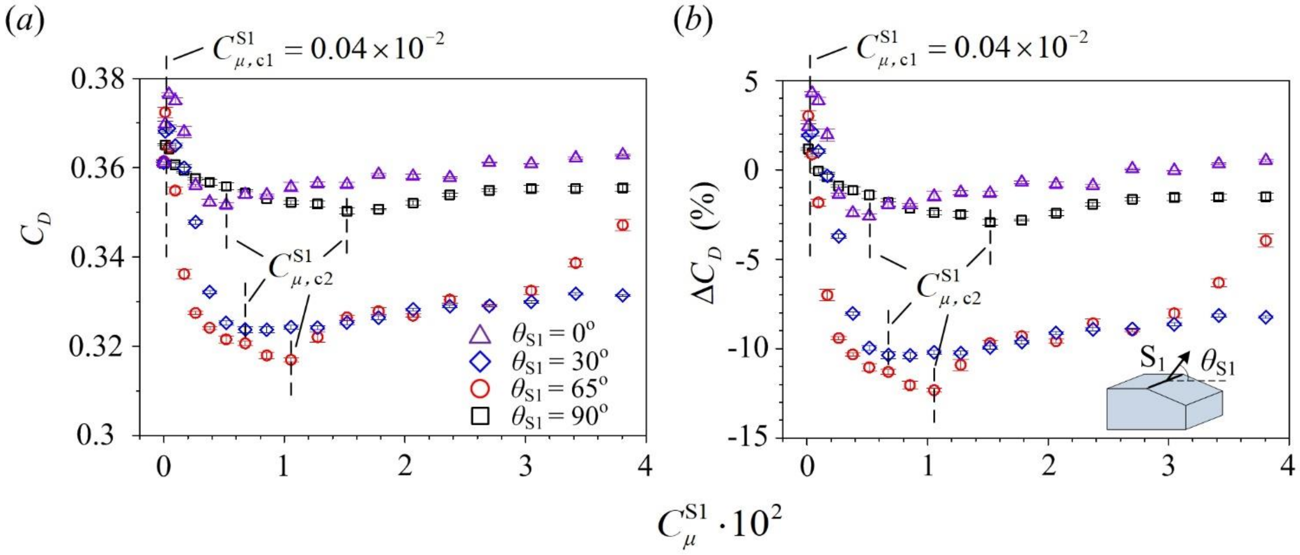

FIGURE 10. Dependence on C^{S1}_{μ} of (*a*) C_D and (*b*) ΔC_D under S_1 at θ_{S1} = 0°, 30°, 65° and 90° for *Re* = 1.7 × 10^5. The uncertainty bars of ΔC_D are determined as the ratio of the uncertainty bars of C_D to $\overline{\overline{C_{D0}}}$. The vertical broken lines indicate the critical momentum coefficients.

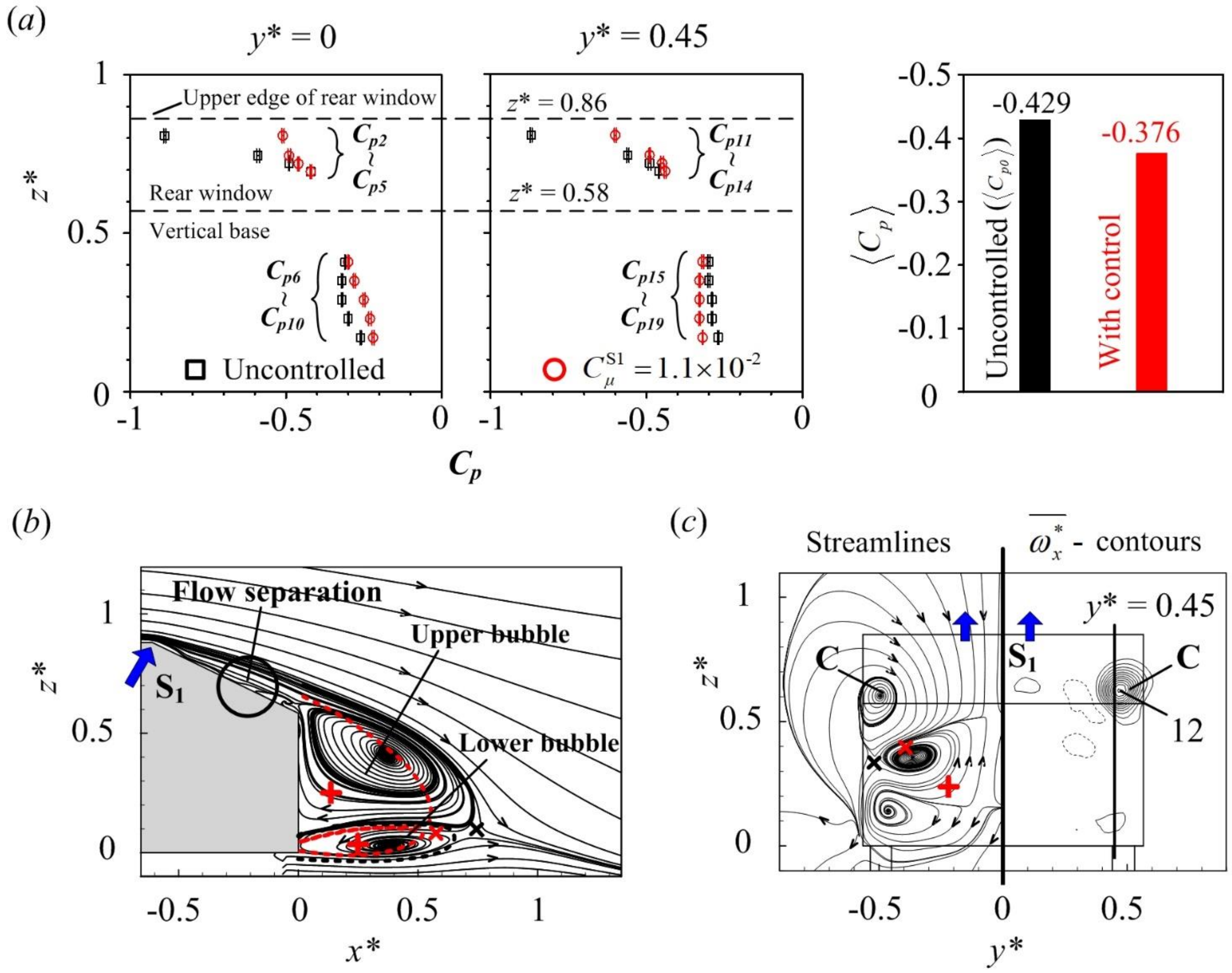

FIGURE 11. (*a*) Variation in C_p on the rear window and the vertical base at $y^* = 0$ and 0.45, and change in $\langle C_p \rangle$, under S$_1$ ($\theta_{S1} = 65°$) at $C_\mu^{S1} = 1.1 \times 10^{-2}$, and the corresponding time-averaged flow structure (*b*) in the (*x*, *z*) plane of $y^* = 0$ and (*c*) in the (*y*, *z*) plane of $x^* = 0.2$. The uncertainty bars of C_p in (*a*) are computed by using $\overline{\overline{\left|C_p - \overline{\overline{C_p}}\right|}}$. Red-colored symbols '×' and '+' in (*b*, *c*) denote the saddle point and the focus, respectively, which are determined from time-averaged streamlines in figures 7(*b*) and 8(*b*). The red-colored broken line in (*b*) indicates the bubble size in the base flow determined from the streamlines in figure 7(*b*). The contour interval and cutoff levels are 1 and ±1, respectively, for $\overline{\omega_x^*}$ in (*c*). $Re = 1.7 \times 10^5$.

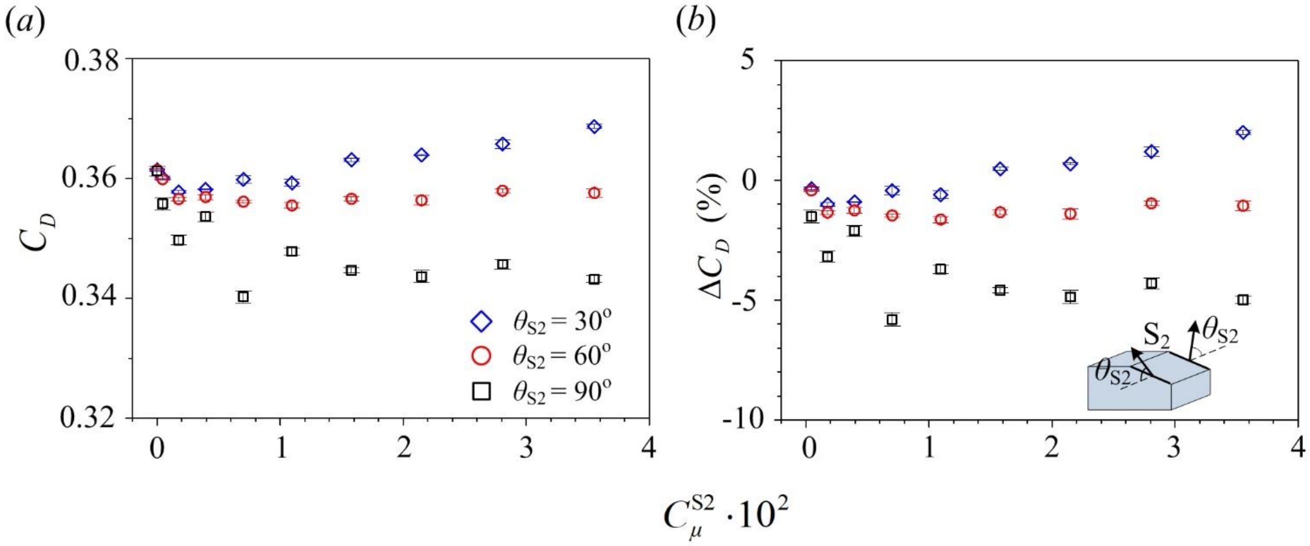

FIGURE 12. Dependence on C_μ^{S2} of (*a*) C_D and (*b*) ΔC_D under S_2 at θ_{S2} = 30°, 60° and 90° for *Re* = 1.7×10^5.

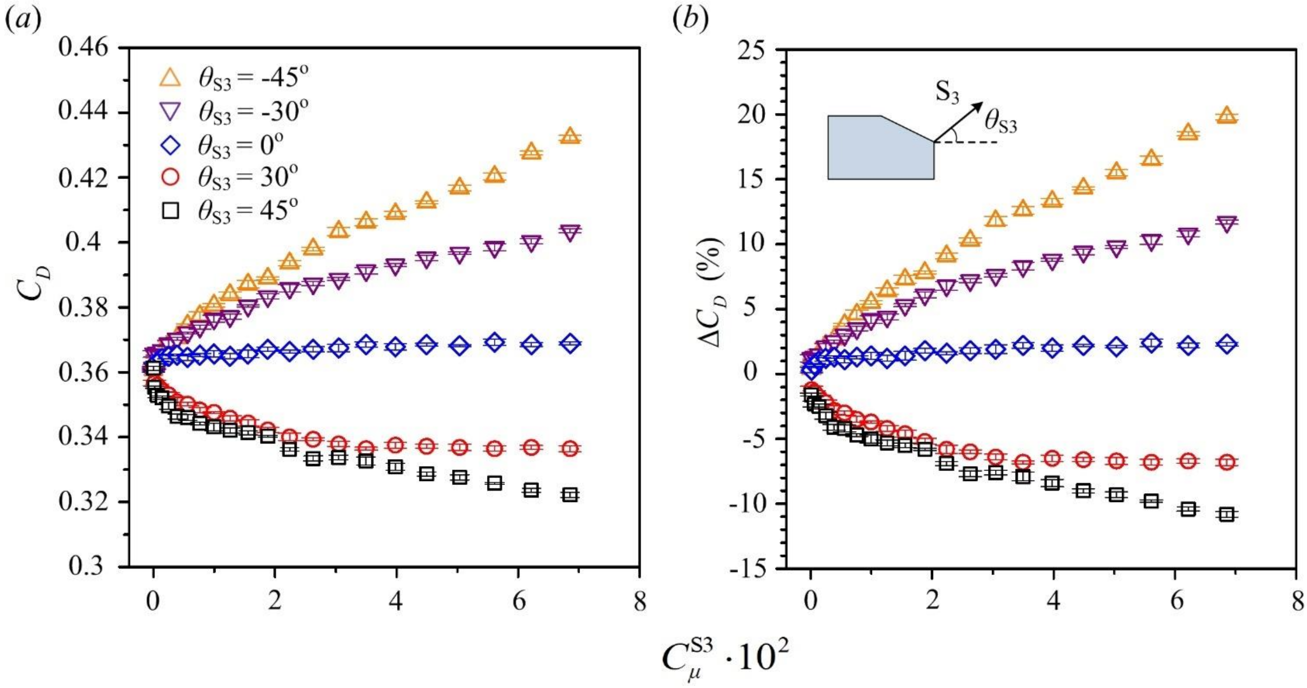

FIGURE 13. Dependence on C_μ^{S3} of (*a*) C_D and (*b*) ΔC_D under S_3 at θ_{S3} = 45°, 30°, 0°, -30° and -45° for $Re = 1.7 \times 10^5$.

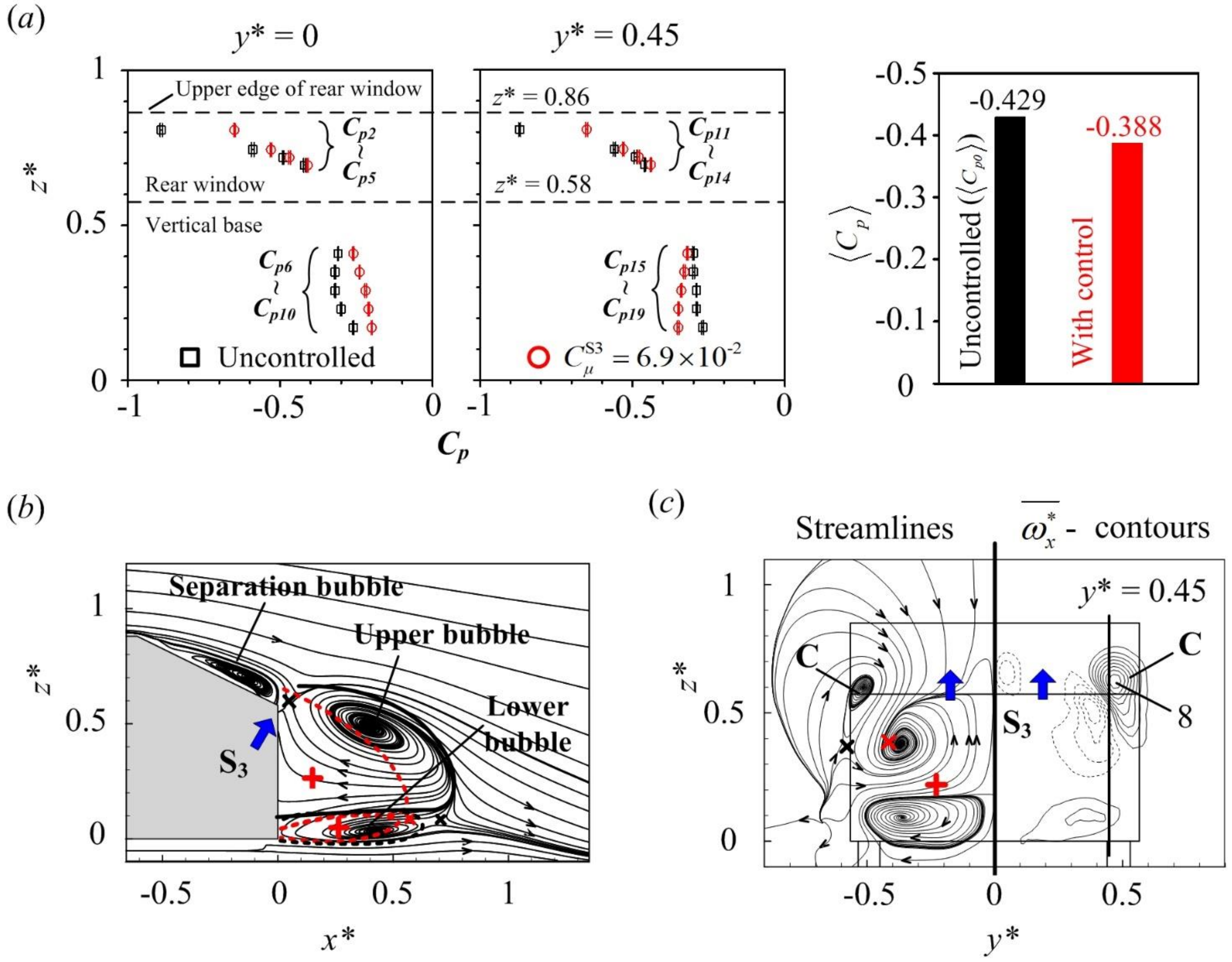

FIGURE 14. (*a*) Variation in C_p on the rear window and the vertical base at $y^* = 0$ and 0.45, and change in $\langle C_p \rangle$, under S$_3$ ($\theta_{S3} = 45°$) at $C_\mu^{S3} = 6.9 \times 10^{-2}$, and the corresponding time-averaged flow structure (*b*) in the (*x*, *z*) plane of $y^* = 0$ and (*c*) in the (*y*, *z*) plane of $x^* = 0.2$. The symbols '×' and '+' and the red-colored broken line in (*b*, *c*) are as in figure 11(*b*, *c*). The contour interval and cutoff levels for $\overline{\omega_x^*}$ in (*c*) are the same as in figure 11(*c*). $Re = 1.7 \times 10^5$.

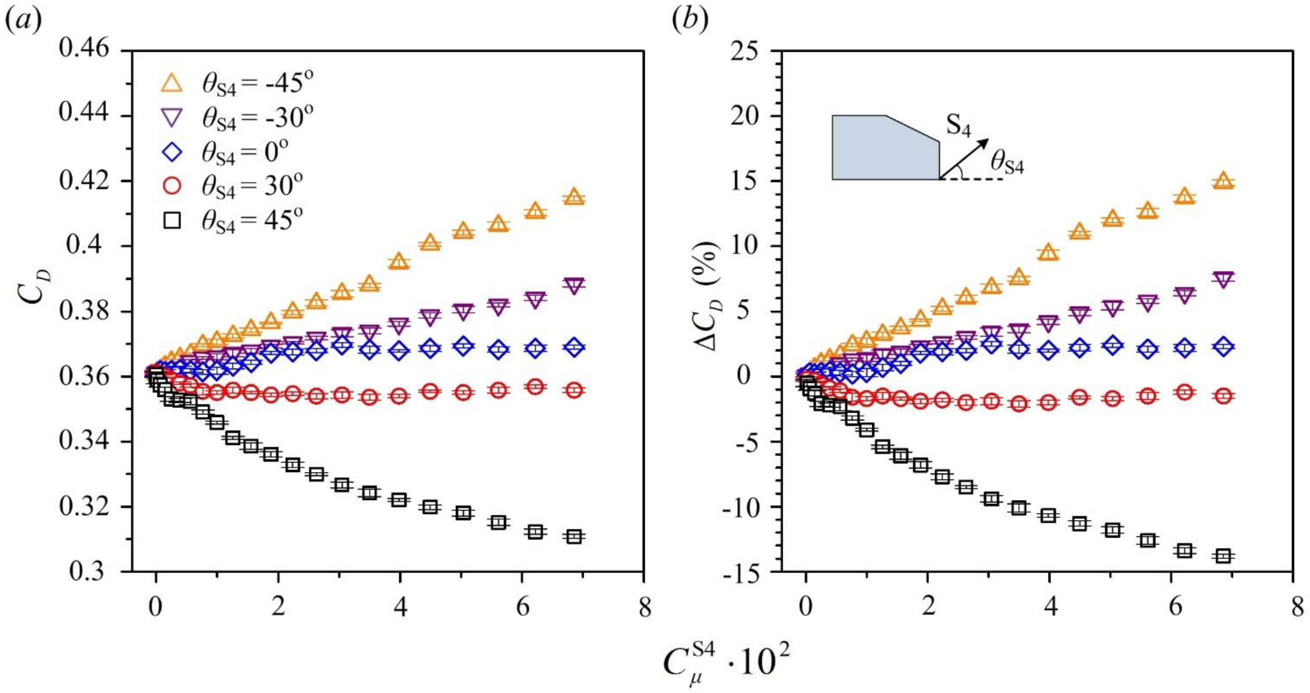

FIGURE 15. Dependence on C_μ^{S4} of (*a*) C_D and (*b*) ΔC_D under S_4 at θ_{S4} = 45°, 30°, 0°, -30° and -45° for $Re = 1.7 \times 10^5$.

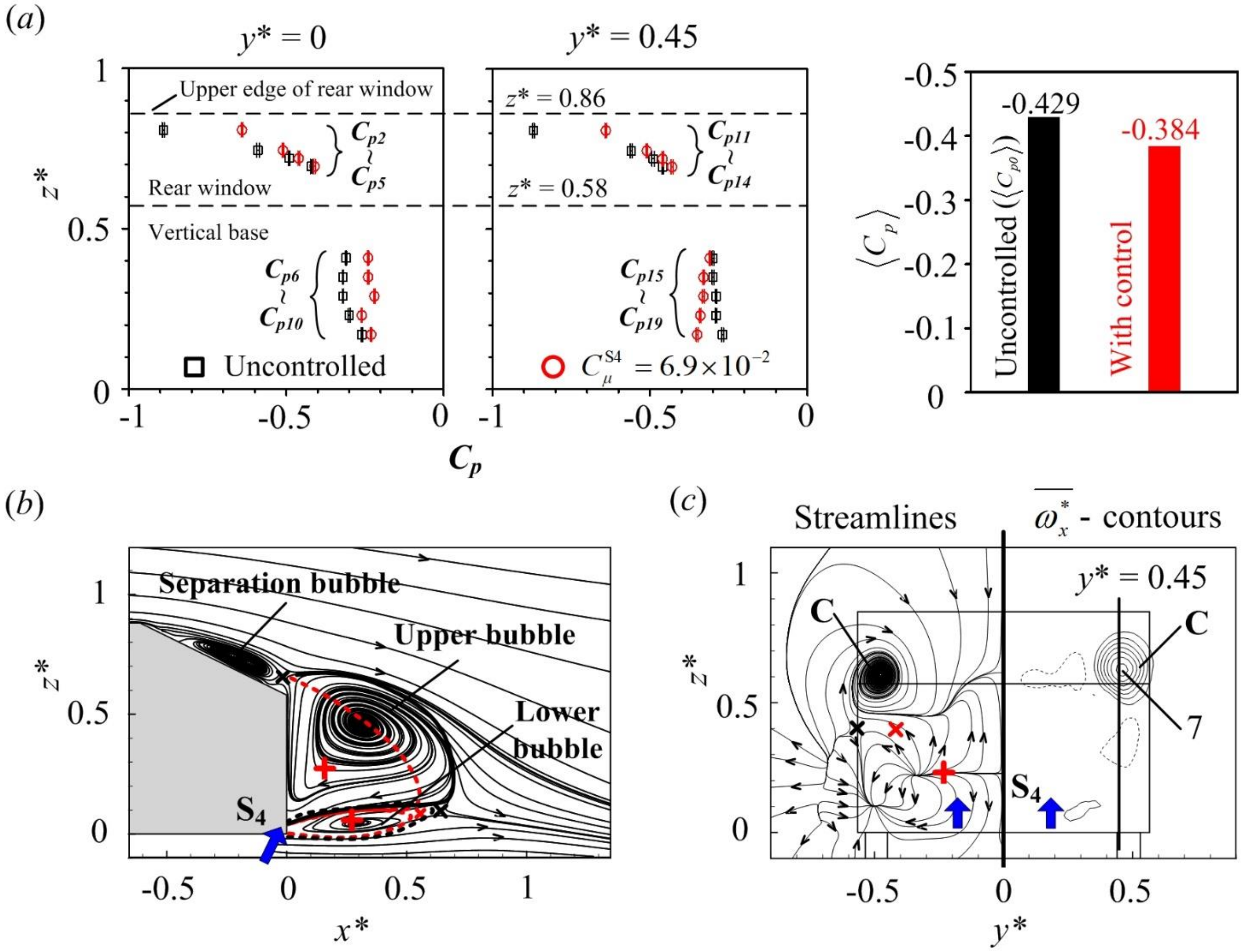

FIGURE 16. (*a*) Variation in C_p on the rear window and the vertical base at $y^* = 0$ and 0.45, and change in $\langle C_p \rangle$, under S4 ($\theta_{S4} = 45°$) at $C_\mu^{S4} = 6.9 \times 10^{-2}$, and the corresponding time-averaged flow structure (*b*) in the (x, z) plane of $y^* = 0$ and (*c*) in the (y, z) plane of $x^* = 0.2$. The symbols '×' and '+' and the red-colored broken line in (*b*, *c*) are as in figure 11(*b*, *c*). The contour interval and cutoff levels for $\overline{\omega_x^*}$ in (*c*) are the same as in figure 11(*c*). $Re = 1.7 \times 10^5$.

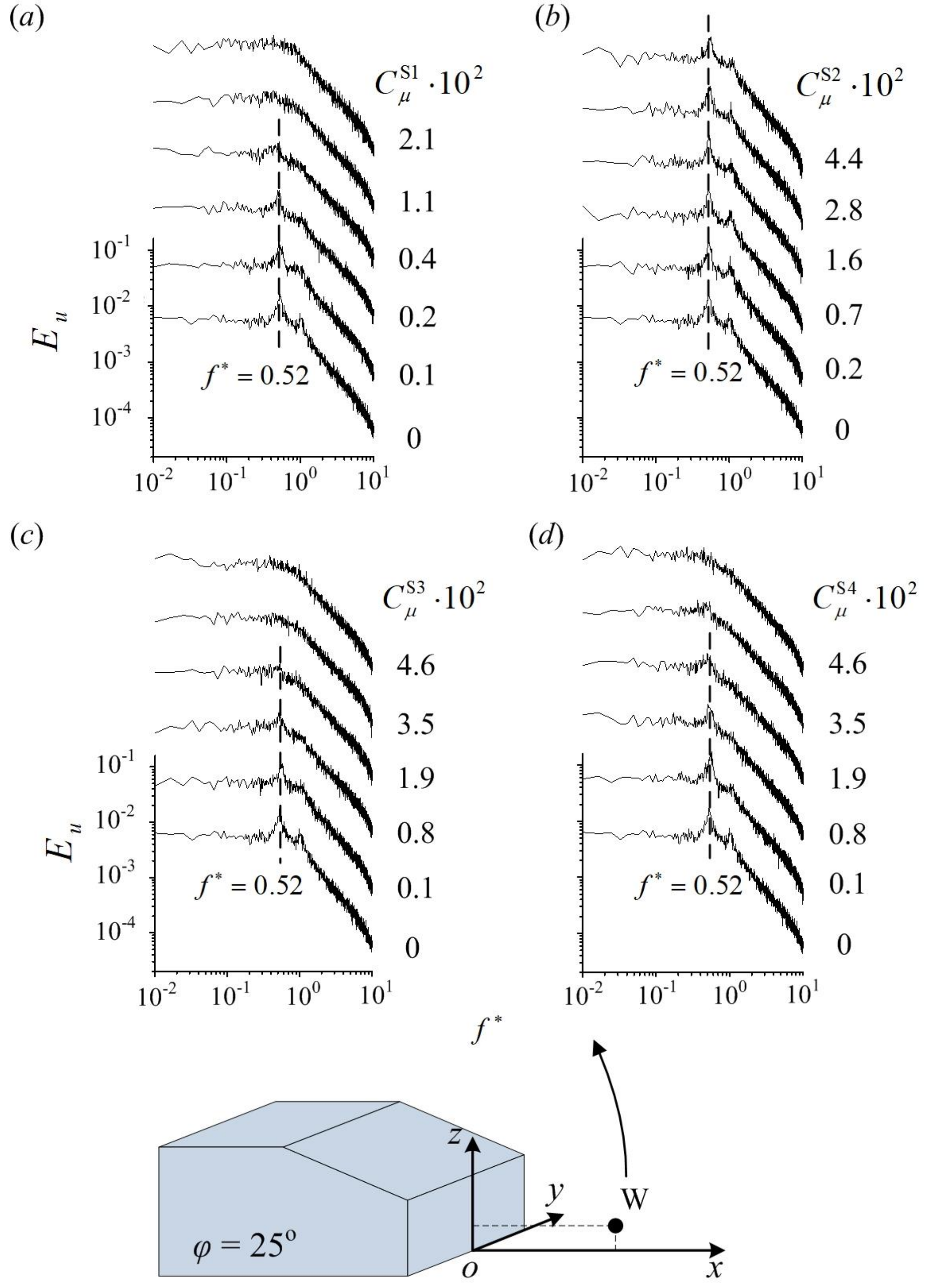

FIGURE 17. E_u measured at W ($x^* = 0.4$, $y^* = 0$, $z^* = 0.18$) under (*a*) S_1 ($\theta_{S1} = 65°$), (*b*) S_2 ($\theta_{S2} = 90°$), (*c*) S_3 ($\theta_{S3} = 45°$) and (*d*) S_4 ($\theta_{S4} = 45°$) for different momentum coefficients. $Re = 1.7 \times 10^5$.

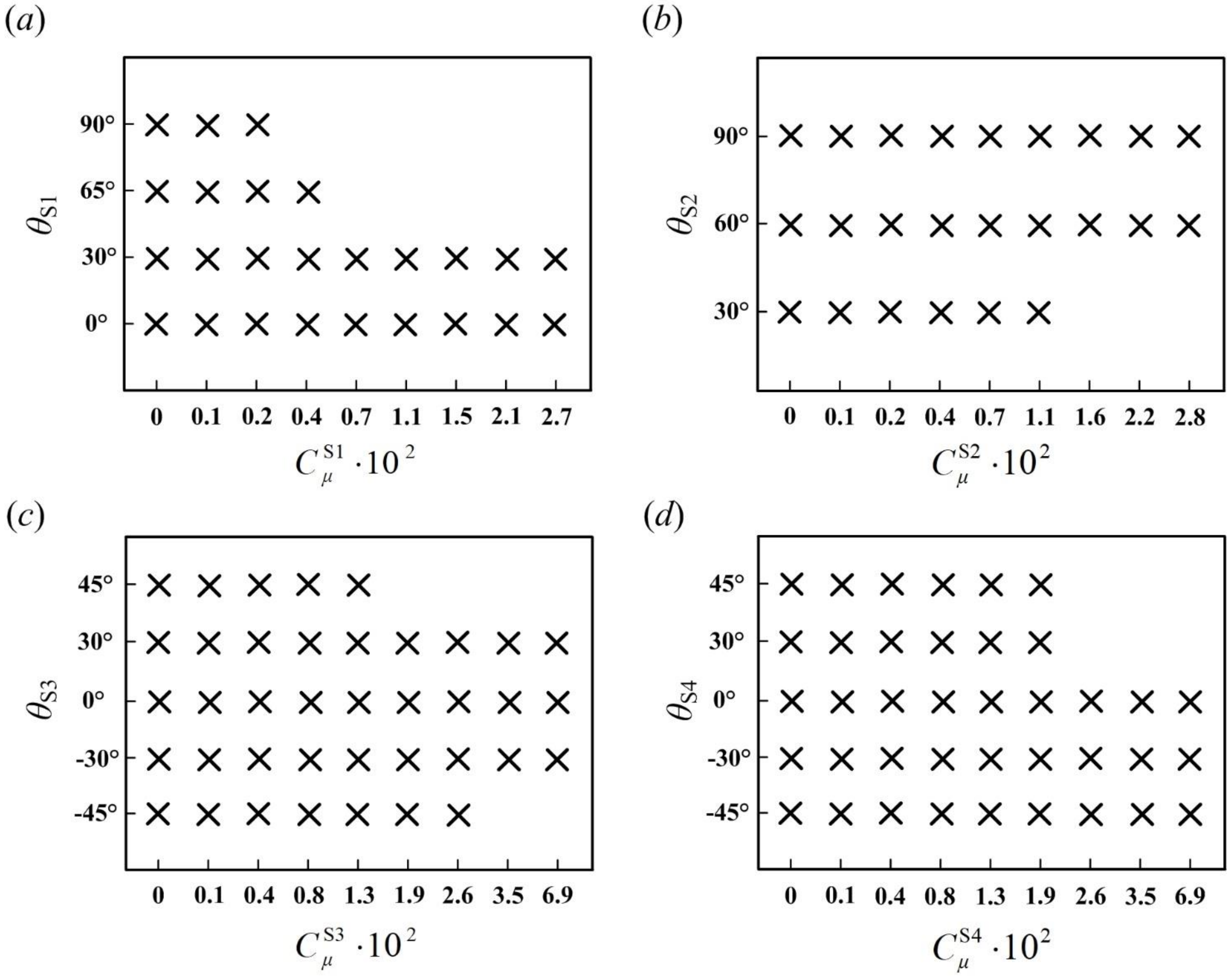

FIGURE 18. Momentum coefficients and blowing angles of (*a*) S_1, (*b*) S_2, (*c*) S_3 and (*d*) S_4, where the predominant vortex frequency ($St = 0.52$) is detected at W. Please refer to figure 17 for the location of W. The symbol '×' denotes the occurrence of the frequency. $Re = 1.7 \times 10^5$.

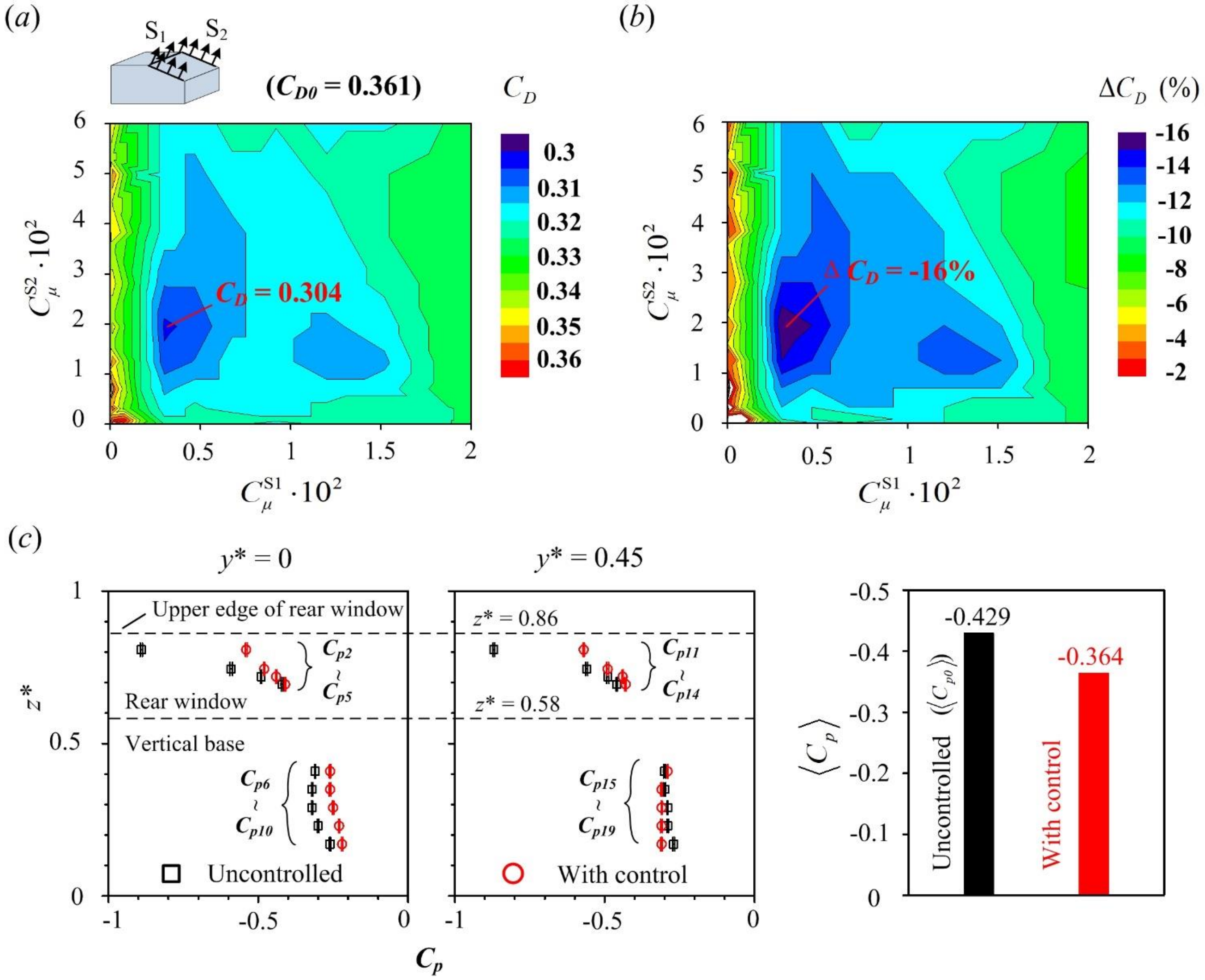

FIGURE 19. Dependence on C_μ^{S1} and C_μ^{S2} of (*a*) C_D and (*b*) ΔC_D under combined S_1 ($\theta_{\mathrm{S1}} = 65°$) and S_2 ($\theta_{\mathrm{S2}} = 90°$). (*c*) Variation in C_p on the rear window and the vertical base at $y^* = 0$ and 0.45, and change in $\langle C_p \rangle$, with the combined actuations at $C_\mu^{\mathrm{S1}} = 0.3 \times 10^{-2}$ and $C_\mu^{\mathrm{S2}} = 2.0 \times 10^{-2}$. $Re = 1.7 \times 10^5$.

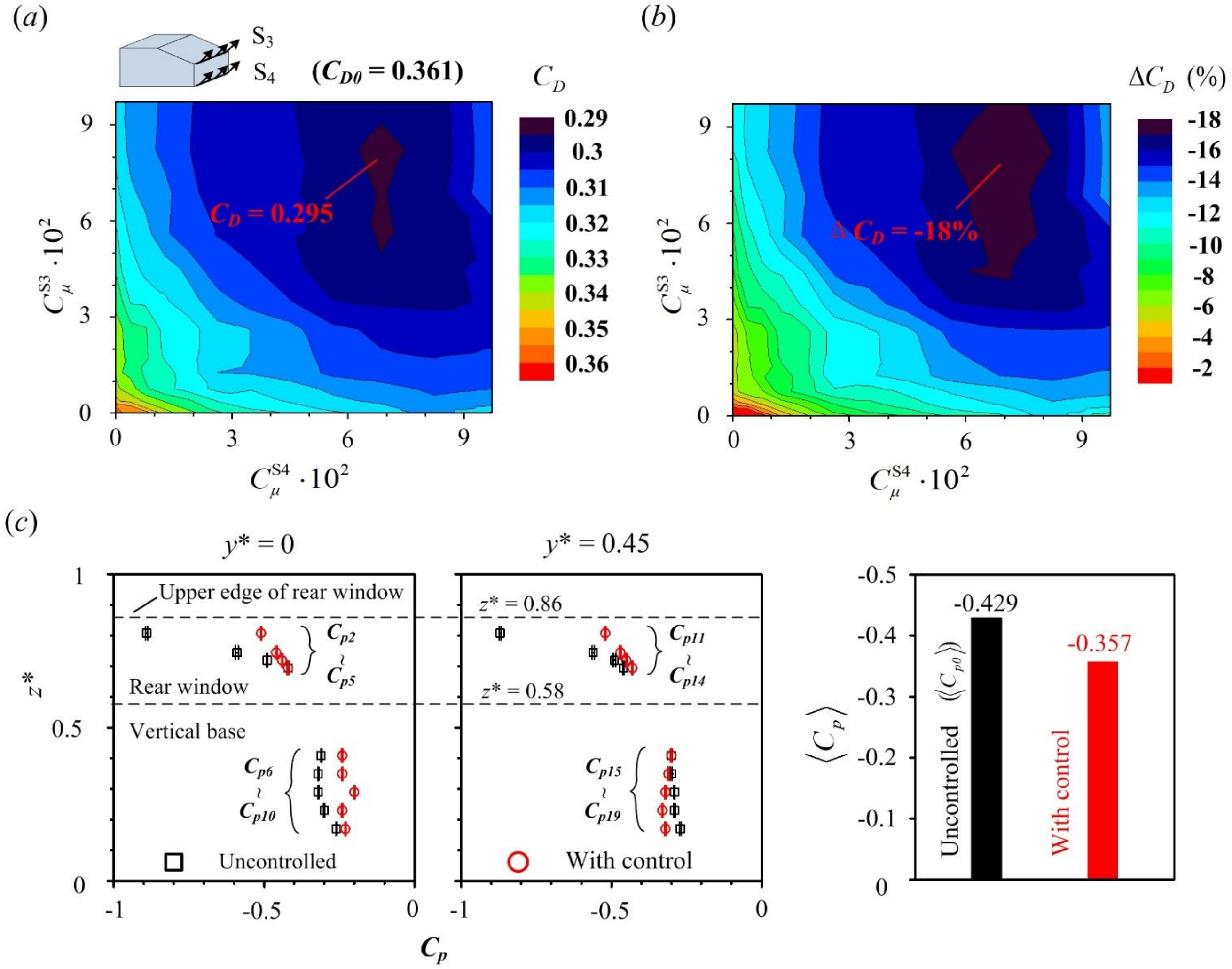

FIGURE 20. Dependence on C_{μ}^{S3} and C_{μ}^{S4} of (*a*) C_D and (*b*) ΔC_D under combined S$_3$ (θ_{S3} = 45°) and S$_4$ (θ_{S4} = 45°). (*c*) Variation in C_p on the rear window and the vertical base at y^* = 0 and 0.45, and change in $\langle C_p \rangle$, with the combined actuations at $C_{\mu}^{S3} = 8.2 \times 10^{-2}$ and $C_{\mu}^{S4} = 6.9 \times 10^{-2}$. $Re = 1.7 \times 10^5$.

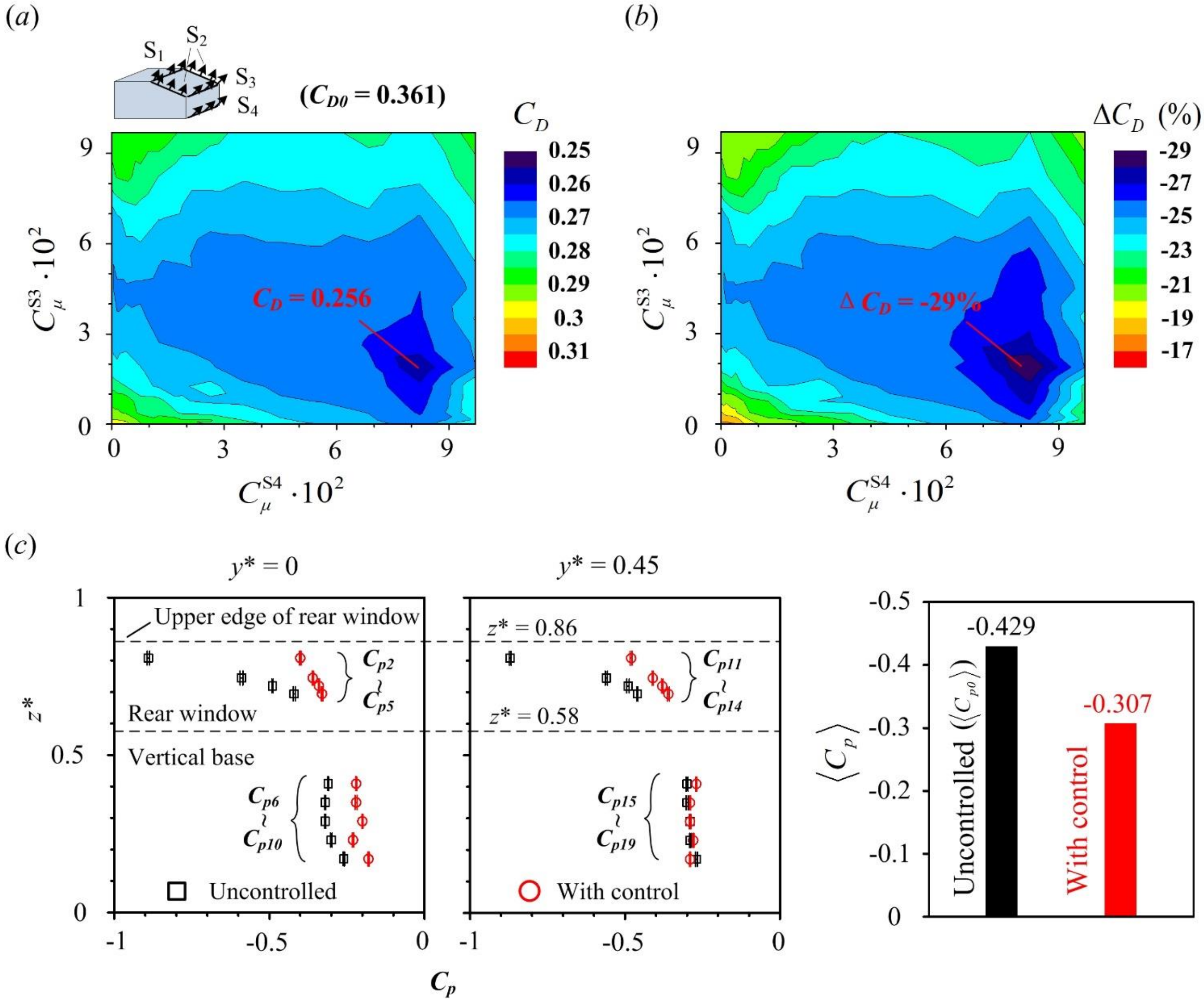

FIGURE 21. Dependence on C_μ^{S3} and C_μ^{S4} of (*a*) C_D and (*b*) ΔC_D under combined S_1 ($\theta_{S1} = 65°$), S_2 ($\theta_{S2} = 90°$), S_3 ($\theta_{S3} = 45°$) and S_4 ($\theta_{S4} = 45°$). (*c*) Variation in C_p on the rear window and the vertical base at $y^* = 0$ and 0.45, and change in $\langle C_p \rangle$, with the combined actuations at $C_\mu^{S1} = 0.3 \times 10^{-2}$, $C_\mu^{S2} = 2.0 \times 10^{-2}$, $C_\mu^{S3} = 1.9 \times 10^{-2}$, $C_\mu^{S4} = 8.2 \times 10^{-2}$. $Re = 1.7 \times 10^5$.

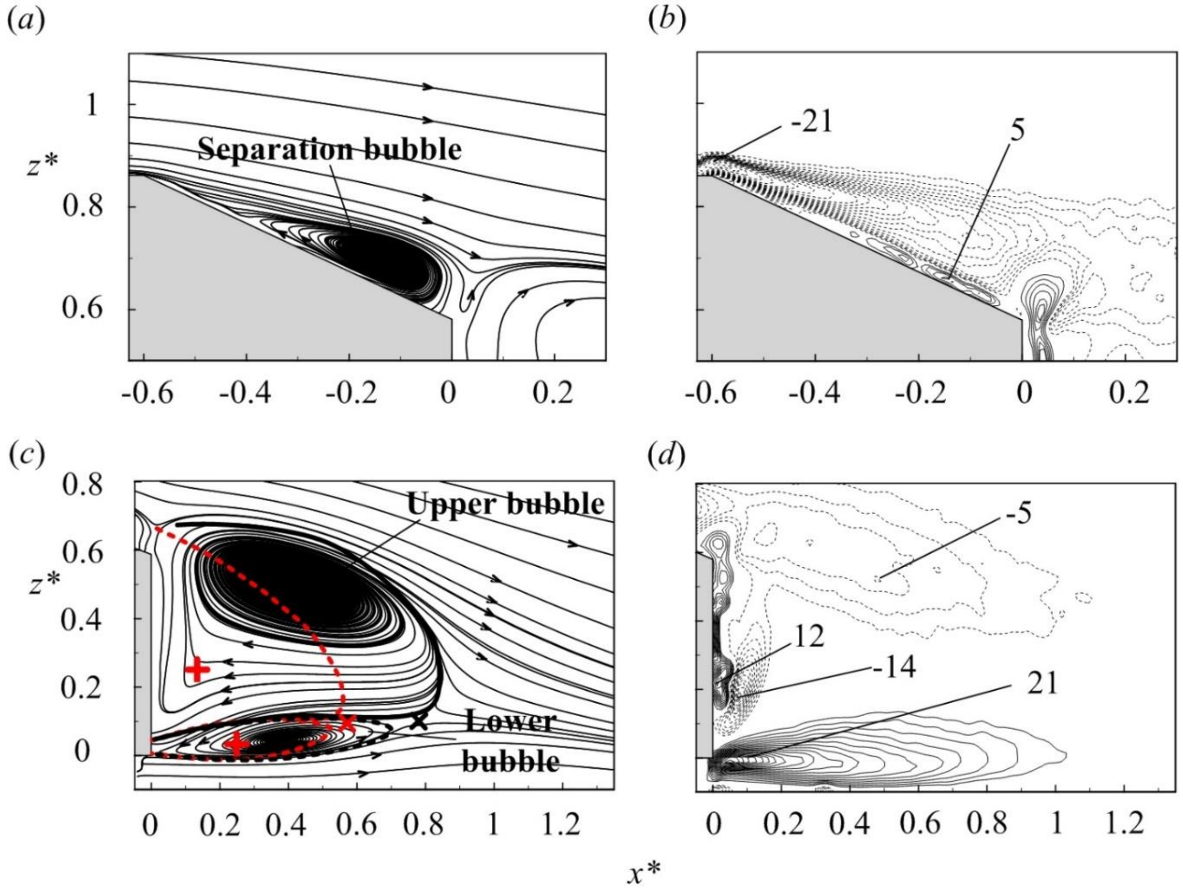

FIGURE 22. (*a*, *c*) Time-averaged streamlines and (*b*, *d*) $\overline{\omega_y^*}$-contours (the contour interval = 1, the cutoff level = ±2) measured in the (*x*, *z*) plane of $y^* = 0$ under the combination of S_1 ($\theta_{S1} = 65°$), S_2 ($\theta_{S2} = 90°$), S_3 ($\theta_{S3} = 45°$) and S_4 ($\theta_{S4} = 45°$). $C_\mu^{S1} = 0.3 \times 10^{-2}$, $C_\mu^{S2} = 2.0 \times 10^{-2}$, $C_\mu^{S3} = 1.9 \times 10^{-2}$ and $C_\mu^{S4} = 8.2 \times 10^{-2}$; symbols '×' and '+' denote the saddle point and the centers; the red-colored broken line indicates the bubble size of the base flow, determined from the time-averaged streamlines shown in figure 7(*b*). $Re = 1.7 \times 10^5$.

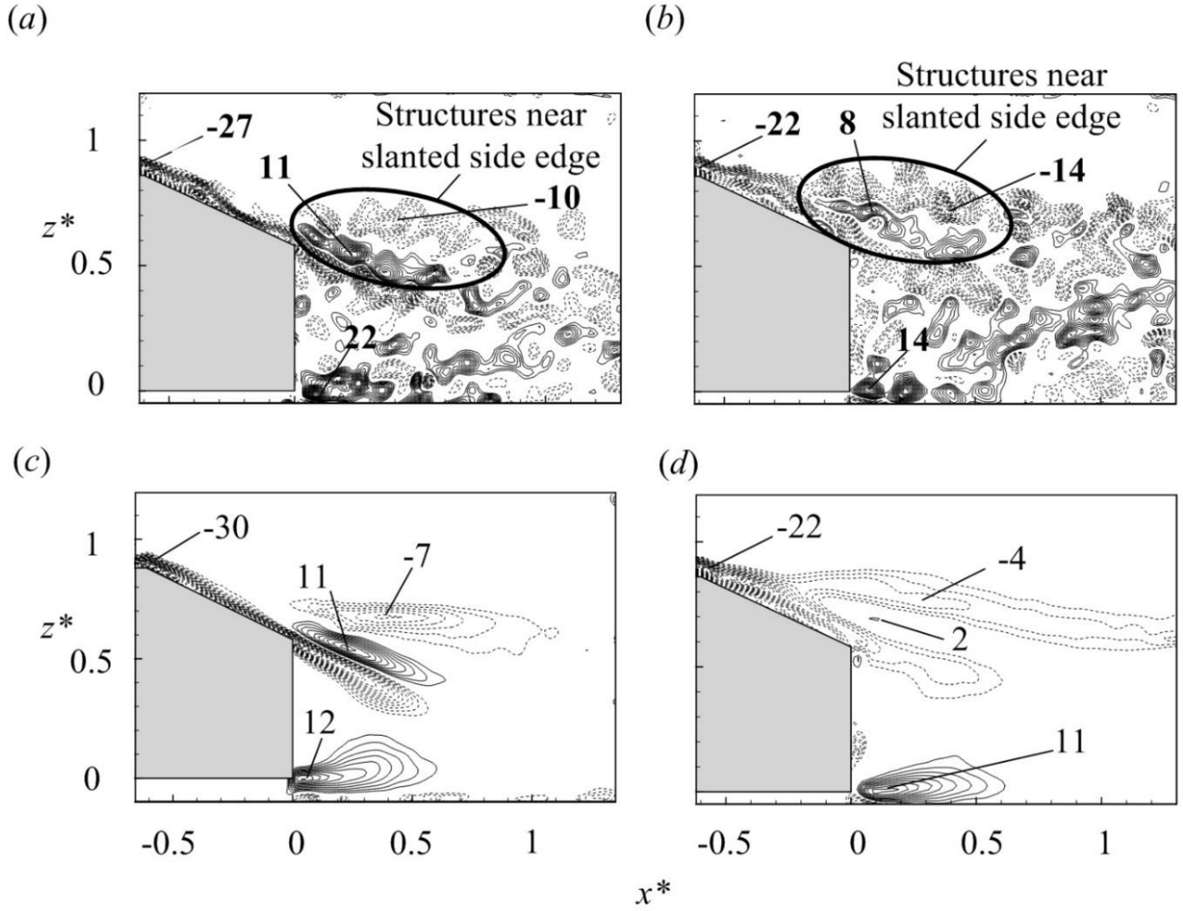

FIGURE 23. Typical instantaneous ω_y^* (*a*, *b*) and $\overline{\omega_y^*}$-contours (*c*, *d*) measured in the (*x, z*) plane of *y** = 0.45: (*a*, *c*) the base flow, (*b*, *d*) under the control of combined S1 (θ_{S1} = 65°), S2 (θ_{S2} = 90°), S3 (θ_{S3} = 45°) and S4 (θ_{S4} = 45°) where $C_\mu^{S1} = 0.3 \times 10^{-2}$, $C_\mu^{S2} = 2.0 \times 10^{-2}$, $C_\mu^{S3} = 1.9 \times 10^{-2}$ and $C_\mu^{S4} = 8.2 \times 10^{-2}$. Contour interval = 1, the cutoff level = ±2. *Re* = 1.7×10^5.

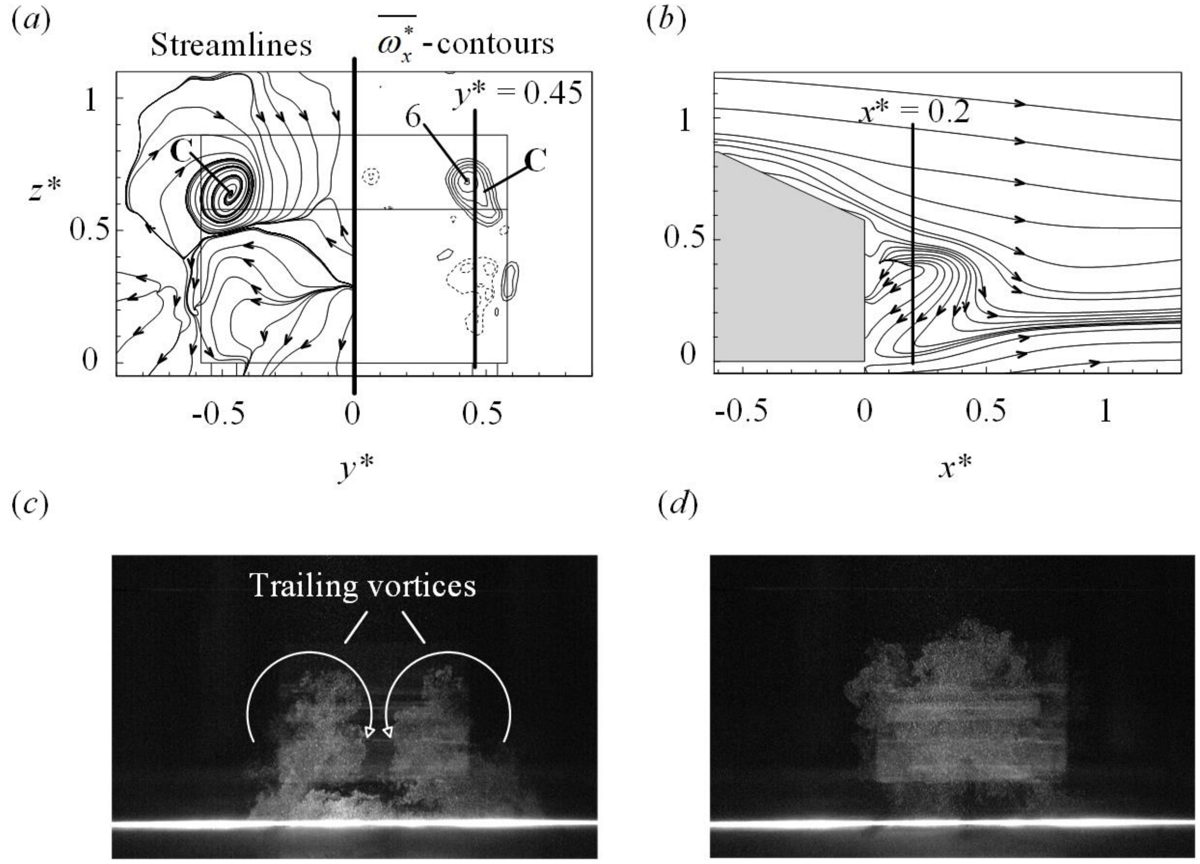

FIGURE 24. (*a*) Time-averaged streamlines and $\overline{\omega_x^*}$-contours in the (*y*, *z*) plane of $x^* = 0.2$ (contour interval = 1, cutoff level = ±1), (*b*) time-averaged streamlines in the (*x*, *z*) plane of $y^* = 0.45$ under the combination of S_1 ($\theta_{S1} = 65°$), S_2 ($\theta_{S2} = 90°$), S_3 ($\theta_{S3} = 45°$) and S_4 ($\theta_{S4} = 45°$). Typical photographs of the flow structure in the (*y*, *z*) plane of $x^* = 1.4$: (*c*) the base flow, (*d*) under control. The white line is the laser light reflection from the floor. $C_\mu^{S1} = 0.3 \times 10^{-2}$, $C_\mu^{S2} = 2.0 \times 10^{-2}$, $C_\mu^{S3} = 1.9 \times 10^{-2}$ and $C_\mu^{S4} = 8.2 \times 10^{-2}$, $Re = 1.7 \times 10^5$.

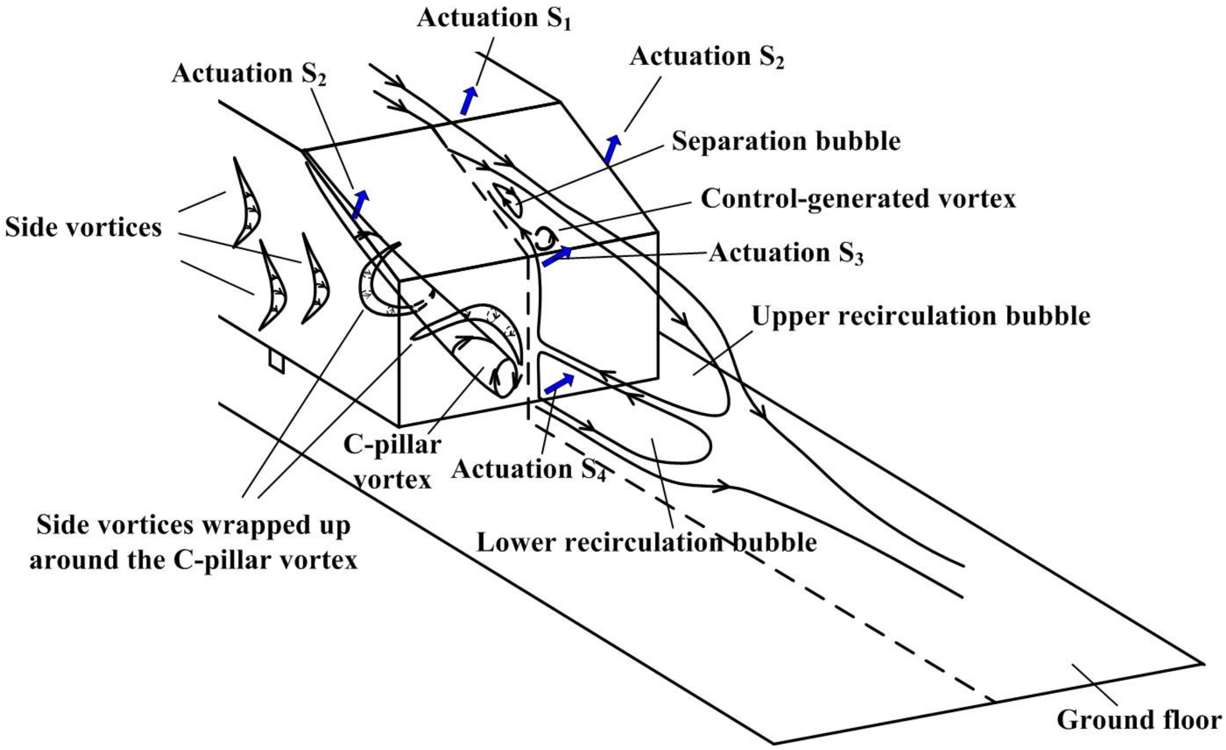

FIGURE 25. Conceptual model of the flow structure under the combined actuation of S_1, S_2, S_3 and S_4.

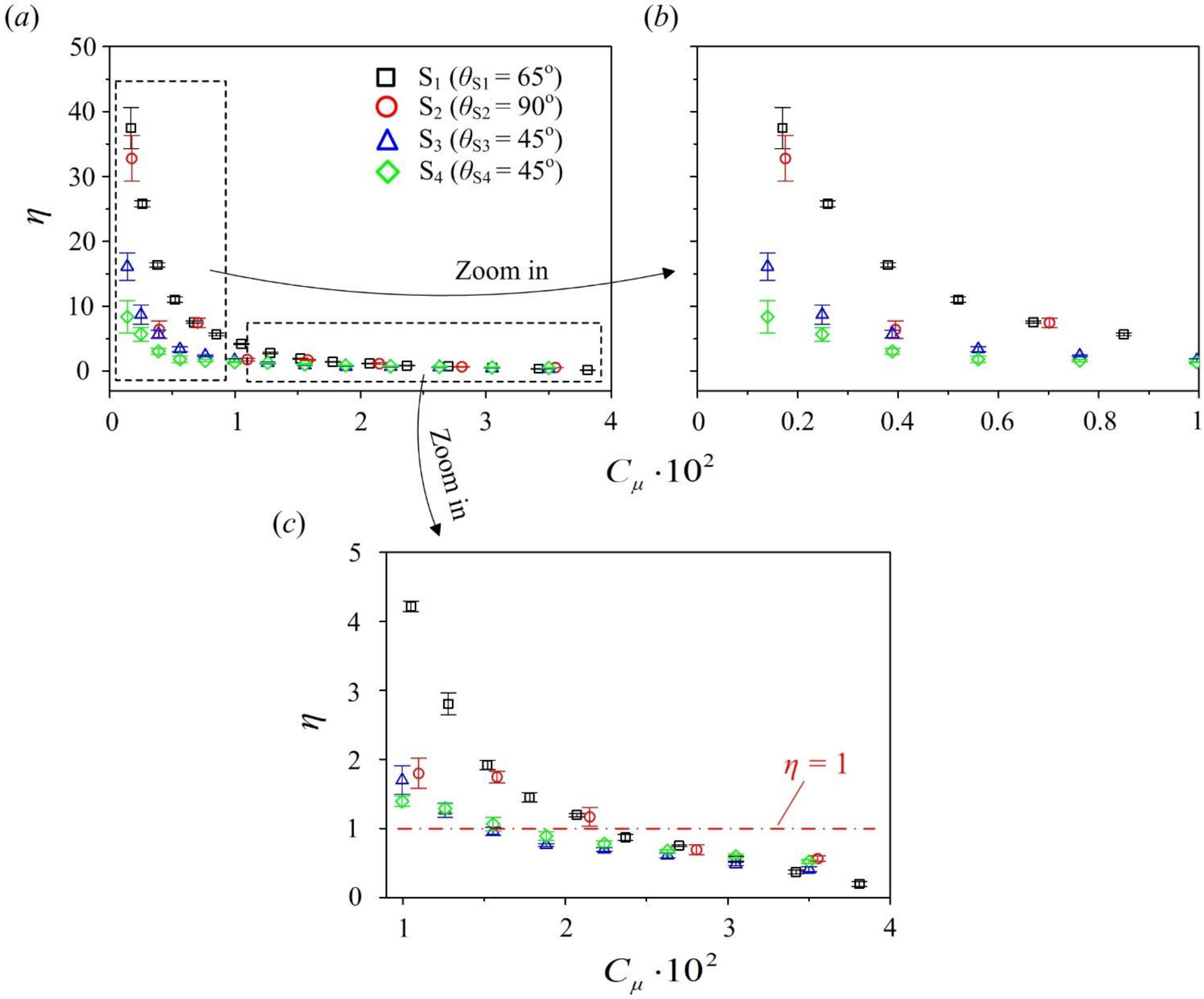

FIGURE 26. (*a*) Dependence of η on C_μ under S$_1$, S$_2$, S$_3$ and S$_4$. (*b*, *c*) Zoom-in plots at $0.1 \times 10^{-2} < C_\mu < 1.0 \times 10^{-2}$ and $1 \times 10^{-2} < C_\mu < 4 \times 10^{-2}$. The uncertainty bars of η are calculated by $\overline{\left|\Delta F_D - \overline{\overline{\Delta F_D}}\right|} \cdot U_\infty / \sum_{i=1}^{4} P_{\mathrm{S}i}$.